Available online at www.sciencedirect.com
SCIENCE DIRECT®
Nuclear Instruments and Methods in Physics Research A 500 (2003) 272–308
NUCLEAR INSTRUMENTS & METHODS IN PHYSICS RESEARCH Section A
www.elsevier.com/locate/nima

Design considerations for thin film coated semiconductor thermal neutron detectors—I: basics regarding alpha particle emitting neutron reactive films

D.S. McGregor[a,*], M.D. Hammig[b], Y.-H. Yang[b], H.K. Gersch[c], R.T. Klann[d]

[a] Department of Mechanical and Nuclear Engineering, Kansas State University, 318 Rathbone Hall, Manhattan, KS 66506, USA
[b] Department of Nuclear Engineering and Radiological Sciences, University of Michigan, Ann Arbor, MI 48109, USA
[c] 105 Briarwood Drive, Versailles, KY 40383-9142, USA
[d] Argonne National Laboratory, 9700 South Cass Avenue, Building 362, Room B-113, Argonne, IL 60439, USA

Received 17 May 2002; received in revised form 20 November 2002; accepted 22 November 2002

Abstract

Semiconductor-based thermal neutron detectors provide a compact technology for neutron detection and imaging. Such devices can be produced by externally coating semiconductor-charged-particle detectors with neutron reactive films that convert free neutrons into charged-particle reaction products. Commonly used films for such devices utilize the $^{10}B(n,\alpha)^{7}Li$ reaction or the $^{6}Li(n,\alpha)^{3}H$ reaction, which are attractive due to the relatively high energies imparted to the reaction products. Unfortunately, thin film or "foil" type thermal neutron detectors suffer from self-absorption effects that ultimately limit neutron detection efficiency. Design considerations that maximize the efficiency and performance of such devices are discussed. Theoretical and experimental results from front coated, back coated, and "sandwich" designs are presented.
© 2002 Elsevier Science B.V. All rights reserved.

PACS: 29.40.W

Keywords: Neutron detector; Semiconductor detector; Radiation detector; Neutron detection

1. Introduction

Since neutrons hold no electronic charge, methods used to recognize neutron interactions within a detector generally rely on second order effects. Two very common neutron interactions that are used for a variety of thermal neutron detectors are the $^{10}B(n,\alpha)^{7}Li$ reaction and the $^{6}Li(n,\alpha)^{3}H$ reaction [1–4] (see Fig. 1). The $^{10}B(n,\alpha)^{7}Li$ reaction leads to the following reaction products [1–4]:

$$^{10}B + {}^{1}_{0}n \rightarrow \begin{cases} {}^{7}Li^{*} \text{ (at 1.015 MeV)} + \alpha \text{ (at 1.777 MeV)}, \\ \text{Reaction } Q\text{-Value} = 2.792 \text{ MeV (to ground state)}, \\ {}^{7}Li^{*} \text{ (at 0.840 MeV)} + \alpha \text{ (at 1.470 MeV)} \\ \text{Reaction } Q\text{-Value} = 2.310 \text{ MeV (1st excited state)} \end{cases}$$

which are released in opposite directions when thermal neutrons (0.0259 eV) are absorbed by ^{10}B. After absorption, 94% of the reactions leave the ^{7}Li ion in its first excited state, which rapidly

*Corresponding author. Tel.: +1-785-532-5284; fax: +1-785-532-7057.
E-mail address: mcgregor@ksu.edu (D.S. McGregor).

0168-9002/03/$ - see front matter © 2002 Elsevier Science B.V. All rights reserved.
doi:10.1016/S0168-9002(02)02078-8

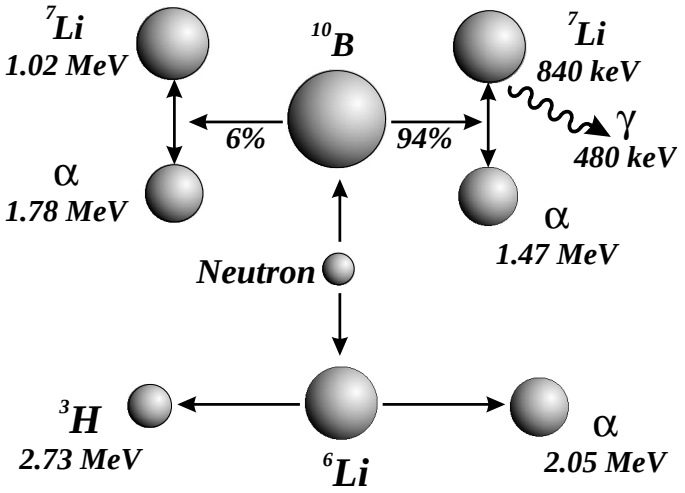

Fig. 1. The two most commonly used neutron reactions for thermal neutron detection purposes are the $^{10}B(n,\alpha)^{7}Li$ reaction and the $^{6}Li(n,\alpha)^{3}H$ reaction.

de-excites to the ground state ($\sim 10^{-13}$ s) by releasing a 480 keV gamma ray. The remaining 6% of the reactions result in the ^{7}Li ion going directly to its ground state. The microscopic thermal neutron absorption cross-section is 3840 b. Additionally, the microscopic thermal neutron absorption cross-section decreases with increasing neutron energy, with a dependence proportional to the inverse of the neutron velocity ($1/v$) over much of the energy range [5,6].

The $^{6}Li(n,\alpha)^{3}H$ reaction leads to the following products:

$$^{6}Li + {}^{1}_{0}n \rightarrow {}^{3}H\ (\text{at } 2.73\ \text{MeV}) + \alpha\ (\text{at } 2.05\ \text{MeV})$$
$$\text{Reaction } Q\text{-Value} = 4.78\ \text{MeV}$$

which again are oppositely directed if the neutron energy is sufficiently small. The microscopic thermal neutron (0.0259 eV) absorption cross-section is 940 b. The thermal neutron absorption cross-section also demonstrates a $1/v$ dependence, except at a salient resonance above 100 keV, in which the absorption cross-section surpasses that of ^{10}B for energies between approximately 150 and 300 keV [5,6]. Additional resonances characteristic to either isotope cause the absorption cross-section to surpass one or the other as the neutron energy increases. Due to its higher absorption cross-section, the $^{10}B(n,\alpha)^{7}Li$ reaction leads to a generally higher reaction probability than the $^{6}Li(n,\alpha)^{3}H$ reaction for neutron energies below 100 keV. However, the higher energy reaction products emitted from the $^{6}Li(n,\alpha)^{3}H$ reaction lead to greater ease of detection than the particles emitted from the $^{10}B(n,\alpha)^{7}Li$ reaction.

There are other neutron reactions that have been used in solid-form films for thermal neutron detectors, including the $^{157}Gd(n,\gamma)^{158}Gd$ reaction [7–11] and the $^{113}Cd(n,\gamma)^{114}Cd$ reaction [12,13], both of which have very large thermal neutron reaction cross-sections. The $^{157}Gd(n,\gamma)^{158}Gd$ reaction leads to the emission of various low energy gamma rays and beta particles, most of which are emitted at energies below 220 keV. The appeal of using ^{157}Gd is due to its large thermal neutron cross-section of 240,000 b [5,6], but the resulting low energy conversion electron and gamma ray emissions can be difficult to distinguish from background gamma rays in a high radiation field. The ^{113}Cd reaction is intriguing as well, with its thermal neutron absorption cross-section of 20,000 b [5,6]. Discreet gamma ray emissions from the $^{113}Cd(n,\gamma)^{114}Cd$ reaction extend beyond 9 MeV, however the salient gamma ray emissions are at 558.6 and 651.3 keV [14,15], which can be discerned with a relatively high resolution gamma ray spectrometer. Unfortunately, any gamma ray spectrometer capable of detecting the

$^{113}Cd(n,\gamma)^{114}Cd$ emissions will also detect any other background gamma rays, which can confuse the measurement.

The neutron detector design discussed in the present work consists of a solid-state detector (or semiconductor diode detector) coated with a solid form of neutron reactive material. Such a device has been often described as a "foil coated" neutron detector, although we adapt the more descriptive name of thin-film-coated neutron detector. Only neutron reactive coatings that liberate high-energy heavy particles from $^{10}B(n,\alpha)^{7}Li$ and $^{6}Li(n,\alpha)^{3}H$ reactions are discussed. The present analysis is also limited to thermal neutron detection, in which the reaction–product distribution is isotropic.

2. The basic concept

Thin film neutron detectors consist of semiconductor diodes, preferably with relatively thin contact layers, upon which a layer (or layers) of neutron reactive material has been deposited. The basic concept has been used by a variety of research groups [16–28]. As shown in Fig. 2, neutrons absorbed in the neutron reactive film release charged-particle reaction products in opposite directions, one of which may enter the semiconductor diode detector. Charged particles entering the detector lose their energy through Coulombic scattering, thereby creating a high-density plasma cloud of columnar ionization in the form of electron–hole pairs. The semiconductor diode detector is voltage biased to separate the electron-hole pairs and drift the charges to their respective contacts. The mobile charges each induce an image charge on the contacts as they move through the device, and the induced charge is integrated and measured by an external pre-amplifier and accompanying electronics.

It is important to note that the charged particles have discrete ranges within a material, and they lose energy as a function of the specific "stopping power" of the material through which they pass [29]. Charged particle energy loss is not linear with distance, and the energy loss for non-relativistic high-energy charged particles can generally be

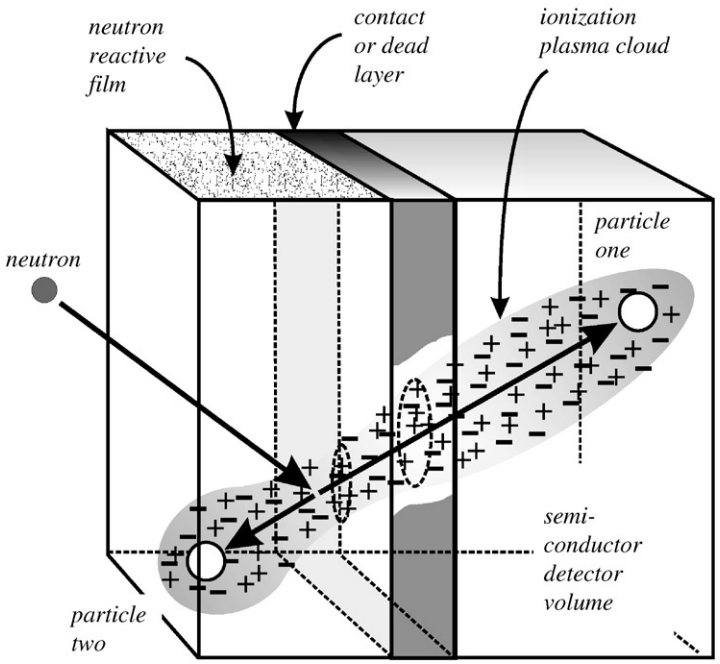

Fig. 2. The fundamental approach to a thin-film-coated semiconductor neutron detector. The film thickness should not exceed the maximum range of the "long-range" reaction product. The reaction products are emitted in opposite directions.

described by the Bethe–Bloche stopping power relation [30]:

$$s = -\frac{1}{N}\frac{dE}{dx} = \frac{4\pi z^2 q^4}{m_0 v^2} Z \ln\left(\frac{2m_0 v^2}{J}\right) \quad (1)$$

where zq and v are the charge and the velocity of the charged particle, N is the atomic density, m_0 is the rest mass of an electron, Z is the material atomic density, and J is an experimentally determined quantity describing the average excitation potential of a representative atom in the material. Although the average range is treated as constant, the actual range fluctuates from particle to particle due to deviations in the number of Coulombic scatters per unit distance and deviations in energy loss per collision. The fluctuation may exceed 5% of the total range, and the deviation is referred to as the "straggle" in the particle range. In the unique case of protons, alpha particles, and other relatively low mass heavy ions, the energy loss as a function of distance can be described by the Bragg ionization curve, in which [29]

$$I(r) = \int_0^{\infty} \frac{i(x-r)}{\beta\sqrt{\pi}} e^{-[(x-R)/\beta]^2}\, dx \quad (2)$$

where x is the range of the individual particle, r is the distance that the particle has traveled in the material, $i(x-r)$ is the specific ionization along the path of the ionizing particle at point $(x-r)$ from the end of its path, R is the mean range and β is the straggling parameter. An interesting characteristic of the Bragg ionization curve for alpha (α) particles is the increase in columnar ionization per unit volume as the ion energy decreases. Hence, the highest density of electron–hole pairs is excited near the end of the range for α-particles. In the present treatment the *average effective range* (denoted L) is the distance through which a particle may *travel within the neutron reactive film* before its energy decreases below the set minimum detectable threshold, typically defined by the electronic lower-level-discriminator (LLD) setting. The term does not take into account additional energy losses from contact "dead regions". L_{SR} and L_{LR} denote the average effective ranges for the short-range and long-range reaction products, respectively.

Neutrons may interact anywhere within the reactive film. From Fig. 2, it is apparent that the reaction products will also lose energy as they move through the reactive film, thus limiting the energy transferred to the semiconductor detector. The finite specific energy loss in the reactive film limits the usable film thickness that can be deposited over the semiconductor device. The voltage signal measured is directly proportional to the number of electron–hole pairs created within the semiconductor. Reaction products that deposit most or all of their energy in the semiconductor volume will produce much larger voltage signals than those reaction products that lose most of their energy in the surface films and contacts.

The neutron flux transmitted through the film as a function of distance x can be described by [31]

$$I(x) = I_0 e^{-x\sigma_F N_F} = I_0 e^{-x\Sigma_F} \quad (3)$$

where I_0 is the initial neutron flux, N_F is the atomic density of the neutron reactive *isotope* in the film, σ_F is the microscopic thermal neutron absorption cross-section of the film, and Σ_F is the film macroscopic thermal neutron absorption cross-section. It is apparent that the fraction of neutrons absorbed in the film through distance x is

$$1 - \frac{I(x)}{I_0} = 1 - e^{-x\sigma_F N_F} = 1 - e^{-x\Sigma_F}. \quad (4)$$

The neutron absorption probability per unit distance is described by [20]

$$p(x)\, dx = \Sigma_F e^{-x\Sigma_F}\, dx. \quad (5)$$

The angular contribution to self-attenuation must also be addressed. Once a neutron is absorbed and the reaction products are emitted, the probability that a reaction product particle will enter the detector is determined by the solid angle subtending the surface within the average effective range (L) of the particle interaction. From Fig. 3, a neutron interaction taking place at distance x from the semiconductor surface has a probability of entering the active volume as described by the

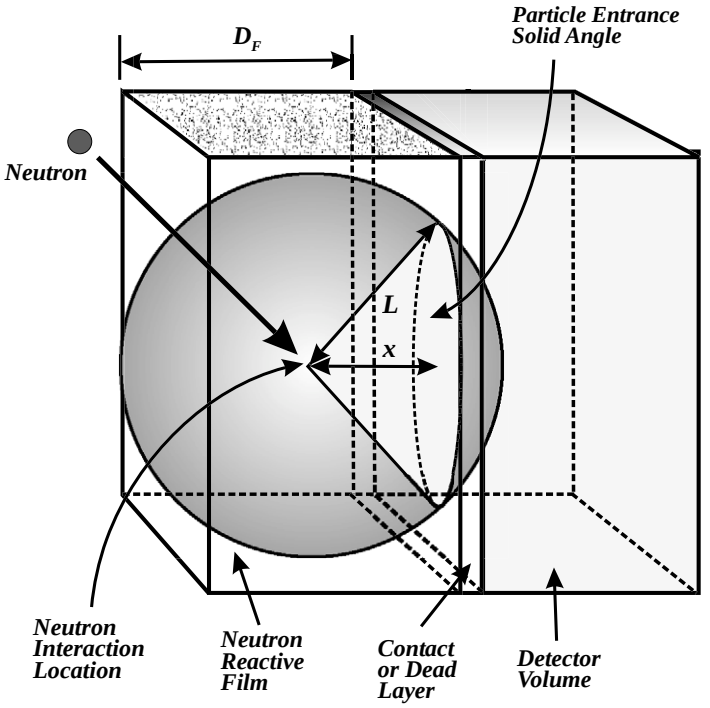

Fig. 3. The solid angle formed by the reaction product ranges that subtends the detector at the interface predetermines the detection probability.

fractional solid angle that subtends the detector,

$$p_{\mathrm{p}}(x) = \frac{\Omega(x)}{4\pi} = \frac{2\pi}{4\pi}\left(1 - \frac{x}{L}\right) = 0.5\left(1 - \frac{x}{L}\right), \quad x \leqslant L \tag{6}$$

where the subscript "p" relates to the reaction product particle of interest. Since the reactions of interest in the present work release two different reaction products per event, the total probability of detecting a neutron reaction consists of adding the detection probabilities of both reaction products. Note that at some interaction locations only one reaction product may be able to reach the semiconductor active volume. Fig. 4 demonstrates the variation in detection efficiency for different neutron interaction depths. Interactions occurring near the detector contact result in either particle entering the detector with high probability as the solid angle approaches 2π. As the neutron interaction distance x increases, the probability of interaction of the short-range particle decreases more rapidly than that of the long-range particle, resulting in an overall decrease in detection sensitivity. At neutron interaction distances greater than L_{LR}, the long-range particle can no longer reach the detector and the neutron absorptions are undetected. Ultimately, it serves no purpose to increase the thickness of the neutron reactive film beyond L_{LR}, as will be shown, and actually works to decrease the overall neutron detection efficiency.

3. Considerations regarding ^{10}B, ^{6}LiF, and ^{6}Li coatings

3.1. ^{10}B coatings

As mentioned previously, the primary ^{10}B(n,α)^{7}Li reaction (94%) results in the emission of a 1.47 MeV alpha particle and a 840 keV ^{7}Li ion in its first excited state, and the ground state reaction results in the emission of a 1.777 MeV

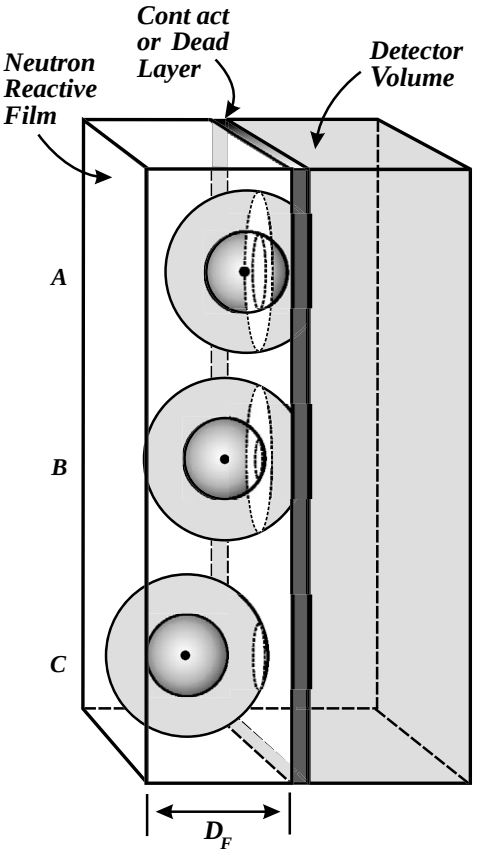

Fig. 4. The solid angle subtending the detector at the interface is greatest for reactions occurring at the film/detector interface. Shown are cases where (A) either particle may enter the detector with high probability, (B) the short-range product has diminished detection probability, and (C) the short-range product will not be detected and the long-range product has diminished detection probability.

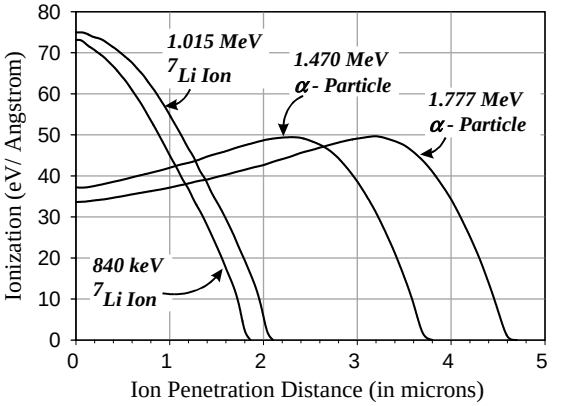

Fig. 5. $^{10}B(n,\alpha)^7Li$ reaction product energy loss in a ^{10}B film as described by the Bragg distribution.

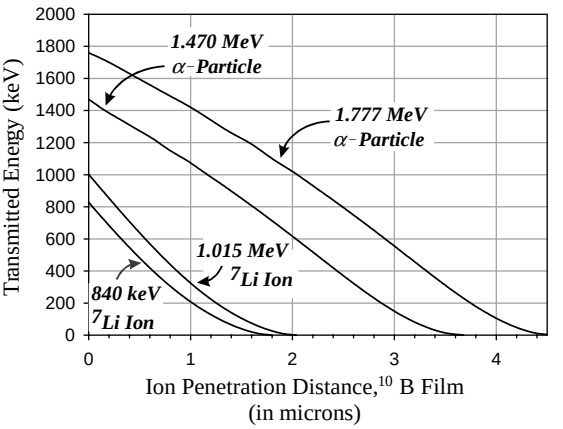

Fig. 6. Energy deposited into the detector is simply the original particle energy minus the energy lost through self-absorption. Shown are the particle energies remaining from the $^{10}B(n,\alpha)^7Li$ reaction as a function of transit distance through pure boron.

alpha particle and a 1.015 MeV ^{7}Li ion. Comparison Bragg ionization curves for both particles within pure ^{10}B film are shown in Fig. 5 [32]. Shown are the calculated range differences for either ion [32], in which the average range for a 0.840 MeV ^{7}Li ion in boron is 1.6 μm and the average range for a 1.47 MeV alpha particle is 3.6 μm.

The energy absorbed in the detector is simply the total energy minus the energy lost in both the boron film and the detector contact during transit. Assuming that energy loss in the detector contact is negligible, Fig. 6 shows the energy retained by either charged particle as a function of interaction distance from the ^{10}B film–detector junction. At any reaction location within the ^{10}B film, the maximum detector entrance energy will be retained by either particle should it enter the detector in an orthogonal trajectory. Hence, if the interaction occurs in the ^{10}B film at a distance of 0.5 μm away from the detector, the maximum energy retained by the ^{7}Li ion will be 430 keV, and the maximum energy retained by the alpha particle will be 1250 keV (see Fig. 6). For the same interaction distance from the detector, the energy retained by the particle when it reaches the

detector active region decreases as the entrance angle changes from orthogonal.

Given a predetermined minimum detection threshold (or LLD setting), the average effective range (L) for either particle can be determined. For instance, from Fig. 6, an LLD setting of 300 keV gives L_{Li} as 0.81 μm and L_{α} as 2.65 μm. The microscopic thermal neutron absorption cross-section (σ) for ^{10}B is 3840 b and the atomic density is 1.3×10^{23} atoms/cm^3. The resulting macroscopic absorption cross-section (Σ) is 500/cm. At 300 keV, the ΣL product for 840 keV ^{7}Li ions is 0.041 and the ΣL product for 1.47 MeV alpha particles is 0.132. Relatively high ΣL products are desirable for improved detection sensitivity. Table 1 lists the ^{10}B(n,α)^{7}Li reaction ΣL products for different detection thresholds.

3.2. ^{6}LiF coatings

The ^{6}Li(n,α)^{3}H reaction emits a 2.73 MeV triton (^{3}H) and a 2.05 MeV alpha particle upon the absorption of a thermal neutron. One popular form of ^{6}Li is the stable compound of ^{6}LiF. The molecular density of ^{6}LiF is 6.12×10^{22} mole-molecules/cm^3, hence the atomic density of ^{6}Li atoms within amounts to the same. The mass density of ^{6}LiF is 2.54 g/cm^3. The microscopic thermal neutron cross-section of ^{6}Li is 940 b, resulting in a macroscopic thermal neutron cross-section of 57.51 cm^{-1}.

Fig. 7 shows the Bragg ionization distributions for the 2.73 MeV triton and the 2.05 MeV alpha particles as they transit through a film of ^{6}LiF. It is apparent that the ranges significantly differ for the two reaction products. The average range for the 2.73 MeV triton in ^{6}LiF is 32.1 μm and the average range for the 2.05 MeV alpha particle in ^{6}LiF is 6.11 μm. Fig. 8 shows the energy retained by either charged particle as a function of interaction distance from the ^{6}LiF film–detector junction. As with the ^{10}B film, the maximum detector entrance energy will be retained by either particle should it transit the ^{6}LiF film and enter the detector in an orthogonal trajectory. From Fig. 8, an LLD

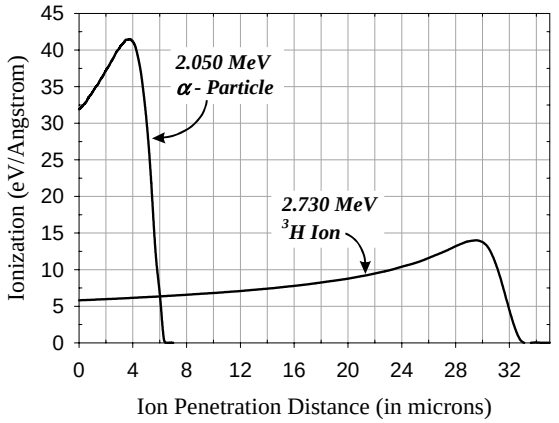

Fig. 7. ^{6}Li(n,α)^{3}H reaction product energy loss in a ^{6}LiF film as described by the Bragg distribution.

Table 1
Calculated average L values and thermal neutron ΣL values for different reaction product particles and minimum energy detection thresholds in a ^{10}B film. The detector entrance dead region was excluded from the calculation, and should be accounted for in cases where dead region absorption is significant

	^{10}B(n,α)^{7}Li Reaction, in ^{10}B, (Σ = 500.00/cm at 0.0259 eV)							
	1.777 MeV α-particle		1.470 MeV α-particle		1.015 MeV ^{7}Li ion		840 keV ^{7}Li ion	
Minimum detection threshold (keV)	L (μm)	ΣL	L (μm)	ΣL	L (μm)	ΣL	L (μm)	ΣL
100	4.0155	0.2008	3.1392	0.1570	1.5148	0.0757	1.2804	0.0640
200	3.7482	0.1874	2.8722	0.1436	1.2527	0.0626	1.0180	0.0509
300	3.5233	0.1762	2.6475	0.1324	1.0453	0.0523	0.8102	0.0405
400	3.3146	0.1657	2.4390	0.1219	0.8667	0.0433	0.6315	0.0316
500	3.1117	0.1556	2.2362	0.1118	0.7055	0.0353	0.4705	0.0235
600	2.9086	0.1454	2.0330	0.1017	0.5548	0.0277	0.3199	0.0160
700	2.7018	0.1351	1.8262	0.0913	0.4110	0.0205	0.1763	0.0881
800	2.4894	0.1245	1.6140	0.0807	0.2720	0.0136	0.0374	0.0187

setting of 300 keV yields L_α as 4.64 μm and L_H as 29.25 μm. At 300 keV, the ΣL product for 2.05 MeV α-particles is 0.027 and the ΣL product for 2.73 MeV tritons is 0.168. Hence, the long-range particle (triton) for the ^{6}Li(n,α)^{3}H reaction in ^{6}LiF gives a higher ΣL product than that realized by the long-range particle (α-particle) for the ^{10}B(n,α)^{7}Li reaction in pure ^{10}B. Conversely, the short-range particle (α-particle) for the ^{6}Li(n,α)^{3}H reaction in ^{6}LiF gives a lower ΣL product than the short-range particle (^{7}Li ion) for the ^{10}B(n,α)^{7}Li reaction in pure ^{10}B. The similar ΣL values for the ^{6}LiF and the pure ^{10}B films indicate that the maximum achievable thermal neutron efficiencies when using these films will differ only slightly. Table 2 lists the ^{6}Li(n,α)^{3}H reaction ΣL products for different detection thresholds and materials

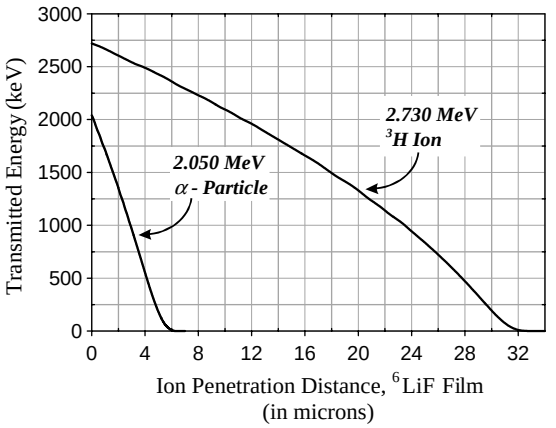

Fig. 8. Energy deposited into the detector is the original particle energy minus the energy lost through self-absorption. Shown are the particle energies remaining from the ^{6}Li(n,α)^{3}H reaction as a function of transit distance through LiF.

3.3. Pure ^{6}Li coatings

Pure ^{6}Li can also be used as a neutron reactive coating, although its corrosive and reactive nature results in cumbersome handling procedures [33]. Pure ^{6}Li has a mass density of 0.463 g/cm^3 and an atomic density of 4.634×10^{22} atoms/cm^3. The macroscopic thermal neutron absorption cross-section is 43.56 cm^{-1}. The low atom density and the low mass density result in rather large reaction product ranges, as can be seen from the Bragg ionization distributions in Fig. 9. Fig. 10 shows the energy retained by either charged-particle reaction product as a function of interaction distance from the ^{6}Li film–detector junction. Clearly, the values of L_{SR} and L_{LR} for the pure ^{6}Li film far surpass those calculated for pure ^{10}B and ^{6}LiF films. Additionally, the resulting ΣL products are greater. For instance, at an LLD setting of 300 keV, the 2.73 MeV triton ΣL product is 0.5532 and the 2.05 MeV alpha particle ΣL product is 0.0828. These high ΣL values allow for, and require, rather

Table 2
Calculated average L values and thermal neutron ΣL values for different reaction product particles and minimum energy detection thresholds in ^{6}LiF and ^{6}Li films. The detector entrance dead region was excluded from the calculation, and should be accounted for in cases where dead region absorption is significant

	^{6}Li(n,α)^{3}H Reaction, in ^{6}LiF (Σ = 57.51/cm at 0.0259 eV)				^{6}Li(n,α)^{3}H Reaction, in ^{6}Li (Σ = 43.56/cm at 0.0259 eV)			
	2.730 MeV Triton		2.050 MeV α-particle		2.730 MeV Triton		2.050 MeV α-particle	
Minimum detection threshold (keV)	L (μm)	ΣL	L (μm)	ΣL	L (μm)	ΣL	L (μm)	ΣL
100	30.754	0.1769	5.3109	0.0305	132.29	0.5762	21.489	0.0936
200	29.958	0.1723	4.9432	0.0284	129.38	0.5636	20.127	0.0877
300	29.239	0.1682	4.6454	0.0267	126.77	0.5522	19.055	0.0830
400	28.523	0.1640	4.3783	0.0252	124.14	0.5408	18.094	0.0788
500	27.783	0.1598	4.2170	0.0238	121.36	0.5286	17.176	0.0748
600	27.005	0.1553	3.8833	0.0223	118.35	0.5155	16.267	0.0709
700	26.185	0.1506	3.6420	0.0209	115.08	0.5013	15.348	0.0669
800	25.320	0.1456	3.4006	0.0196	111.57	0.4860	14.409	0.0628

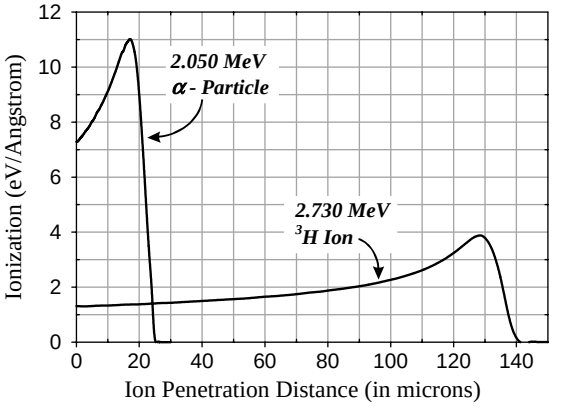

Fig. 9. $^{6}Li(n,\alpha)^{3}H$ reaction product energy loss in a pure ^{6}Li film as described by the Bragg distribution.

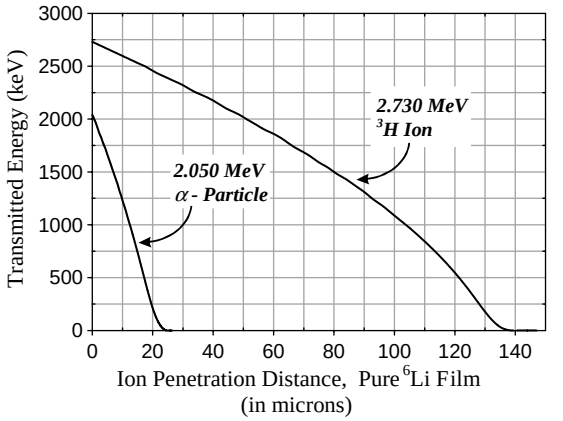

Fig. 10. Energy deposited into the detector is the original particle energy minus the energy lost through self-absorption. Shown are the particle energies remaining from the $^{6}Li(n,\alpha)^{3}H$ reaction as a function of transit distance through pure Li.

thick reaction product films, with $L_\alpha = 19.05\,\mu m$ and $L_H = 126.77\,\mu m$. Such thick ^{6}Li films can be difficult to apply as well as protect from chemically decomposing [33].

4. Devices coated on a single surface

4.1. Front side irradiation—the general 3-dimensional surface

Although the semiconductor and film surfaces will typically be planar, theoretically they can take on any functional form. In order to determine the optimal configuration for a thin film neutron detector, it is instructive to calculate the detection efficiency for a general surface.

For the sake of simplicity, the following assumptions are made:

(i) Assume that the macroscopic neutron absorption cross-section (Σ) is independent of the incident neutron energy. This assumption implies that the incident neutrons are monoenergetic or that the interactions can be acceptably modeled with an average macroscopic cross-section ($\Sigma = \Sigma_{ave} = \Sigma[E_{ave}]$).
(ii) Assume that the neutron undergoes at most one interaction in the film.
(iii) Assume that only one ion is produced from the neutron interaction, noting that the following formulation can be easily extended to multiple reaction products.
(iv) Neglect charged-particle energy straggling, so that the average effective range (L) of the ion reaction product is constant.
(v) Assume that the neutron reactive film thickness (D_F) is less than L.
(vi) Assume that the emission of the ion is uniformly distributed in angle. Such an assumption is reasonably accurate for thermal neutrons, but inaccurate for neutrons of appreciable energy.
(vii) Assume that the probability of neutron capture and the probability that an ion enters the active detector volume are independent.

Consider the general three-dimensional surface, S, of the form $z = f(x, y)$, as shown in Fig. 11. An incoming neutron will produce a measurable detector signal if the following two events occur. First, the neutron must interact in the conversion layer and produce one or more charged particles. Second, the reaction product charged particles must enter the detector volume to excite electron–hole pairs. In the following section, the probability that a reaction product ion will enter the active volume, following a neutron capture at point (x', y', z'), is first derived. The probability of a neutron interacting within the converter film is then developed.

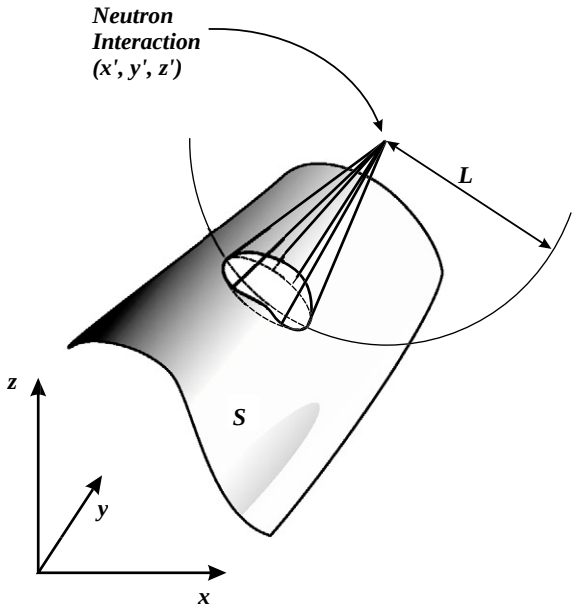

Fig. 11. Three-dimensional surface (S) with function $z = f(x, y)$ with neutron interaction reaction products within range of intersecting the surface.

Deriving the ion impact probability amounts to calculating the fractional solid angle subtended by the surface that is within the average effective range (L) of the interaction point, as shown in Fig. 11. It is advantageous to first find the point $(x_s, y_s, f(x_s, y_s))$ on surface S through which a normal vector to S passes and intersects the interaction point (x', y', z'). The normal vector to a surface, $f(x, y)$, is given by

$$\hat{\boldsymbol{n}} = \frac{1}{\sqrt{1 + f_x^2 + f_y^2}}\left[-f_x\hat{\boldsymbol{i}} - f_y\hat{\boldsymbol{j}} + \hat{\boldsymbol{k}}\right] \tag{7}$$

where f_x and f_y are the partial derivatives of f with respect to x and y. Consider the projection of the normal vector into the (z, x)-plane. The *magnitude* of the slope of the resulting projection is given by $(-1/f_x)$. Recognizing that the line passes through the projection of the interaction point, (x', z') and the projection of the surface interaction point, $(x_s, f(x_s, y_s))$, the line equation can be used to write (x_s, y_s) in terms of (x', z') as

$$f(x_s, y_s) = z' + \frac{x' - x_s}{f_x(x_s, y_s)}. \tag{8}$$

Similarly, the projection of the normal vector in the (z, y)-plane yields

$$f(x_s, y_s) = z' + \frac{y' - y_s}{f_x(x_s, y_s)}. \tag{9}$$

Eqs. (8) and (9) may then be solved for the surface point (x_s, y_s) through which the unit normal passes. Note that depending on the form of S, Eqs. (8) and (9) may yield multiple solutions of (x_s, y_s) as illustrated in Fig. 12.

In order to calculate the angle subtended by the surface, the point of intersection between the vector $\boldsymbol{L}^{\rightarrow}$ (with base at (x', y', z')) and surface S must be found for all (x, y). The calculations are simplified by forming a cylindrical polar reference frame, (r, ϕ, z), centered at $(x_s, y_s, f(x_s, y_s))$ with the z-axis parallel to that in the base frame of (x, y, z) (see Fig. 13). The intersection between $\boldsymbol{L}^{\rightarrow}$ and the surface thus occurs at r_R, as given by Eq. (10), in terms of derived (x_s, y_s) and known $(x', y', z',$ *and* $\phi)$ quantities,

$$L^2 = (x' - (x_s + r_R\cos\phi))^2 + (y' - (y_s + r_R\sin\phi))^2 + (z' - f(x_s + r_R\cos\phi, y_s + r_R\sin\phi))^2. \tag{10}$$

The distances d and l can also be derived from the points defined in Fig. 13, as shown in Eqs. (11) and (12):

$$d^2 = (x' - x_s)^2 + (y' - y_s)^2 + (z' - f(x_s, y_s))^2 \tag{11}$$

and

$$l^2 = r_R^2 + (f(x_s + r_R\cos\phi, y_s + r_R\sin\phi) - f(x_s, y_s))^2. \tag{12}$$

From the law of cosines, the desired angle α is therefore given by

$$\cos\alpha = \frac{d^2 + L^2 - l^2}{2dL}. \tag{13}$$

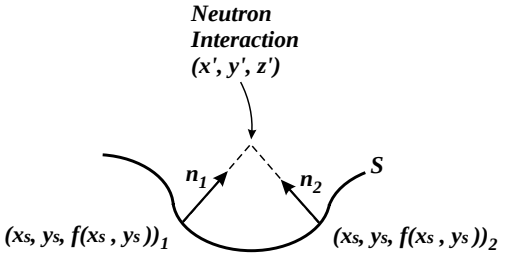

Fig. 12. More than one solution for the normal point is possible with curved surfaces.

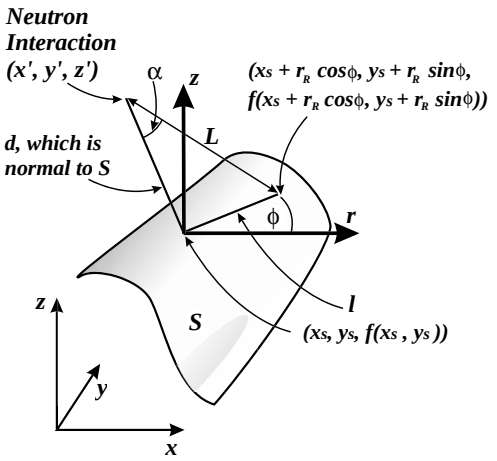

Fig. 13. Cylindrical coordinate system, showing the reference system for a neutron interaction occurring near the surface, S.

If A_p is defined as the area of the converter film projected into the (x, y)-plane, then the detection efficiency can be written as

$$\varepsilon = \frac{1}{A_p}\int\int_{A_p} dx\,dy \int_{f(x,y)}^{f(x,y)+D} dz\ \Sigma e^{-\Sigma(D+f(x,y)-z)} \times \left[\frac{\int_0^{2\pi} d\phi \int_0^{\alpha} d\theta \sin\theta}{4\pi}\right] \quad (14a)$$

or

$$\varepsilon = \frac{1}{A_p}\int\int_{A_p} dx\,dy \int_{f(x,y)}^{f(x,y)+D} dz\ \Sigma e^{-\Sigma(D+f(x,y)-z)} \times \left[\frac{\int_0^{2\pi} d\phi(1-\cos\alpha)}{4\pi}\right] \quad (14b)$$

where

$$D = D_F\left[1 + f_x^2 + f_y^2\right]^{1/2}. \quad (15)$$

The part of the integral inside the brackets in Eqs. (14a) and (14b) is independent of the neutron trajectory. However, the attenuation integral (in z) assumes that the neutron beam is parallel and aligned along the z-axis. Furthermore, the converter layer is assumed to conform to the shape of the underlying surface. The method described in this section as well as the analytical results can be used to calculate the theoretical efficiency for various converter film morphologies of interest. In the following sections some simple configurations will be examined.

4.2. Front side irradiation—the uniformly coated planar case

A commonly used geometry involves the use of a planar semiconductor detector on which a neutron reactive film has been deposited. For such a device, the boundary conditions are:

(i) The neutron reactive films coating the device are uniform and conformal.
(ii) The device surface is void of morphological imperfections.
(iii) The device plane is situated perpendicular to a neutron beam.
(iv) The lateral dimensions of the detector are large compared to the maximum charge particle ranges within the reactive film.
(v) The source neutrons are of low enough energy such that kinetic energy effects are negligible. In other words, the reaction products are emitted opposite each other at an angle of 180°.

The coordinate system shown in Fig. 14 is adapted for the following analysis. It is assumed that the contact thickness (D_1) is negligible. Eq. (3) becomes

$$I(x) = I_0 e^{-\Sigma_F(D_F - x)} \quad (16)$$

where D_F is the converter film thickness and I_0 is the initial neutron beam intensity before entering the reactive film. Additionally, Eq. (5) becomes

$$p(x)\,dx = \Sigma_F e^{-\Sigma_F(D_F - x)}\,dx. \quad (17)$$

The sensitivity contribution for a reaction product particle can be found by integrating over the product of the interaction probability (Eq. (17)) and the fractional solid angle through film thickness D_F. The efficiency can equivalently be derived from the framework described in Section 4 above. If the surface, S, is parameterized as $f(x, y) = 0$ for all x, y, then Eq. (14b) reduces to:

$$S_p(D_F) = \frac{F_p}{4\pi I_0}\int_0^{D_F} I_0 2\pi\Sigma_F e^{-\Sigma_F(D_F - x)}\left(1 - \frac{x}{L}\right)dx = 0.5F_p\left\{\left(1 + \frac{1}{\Sigma_F L}\right)(1 - e^{-\Sigma_F D_F}) - \frac{D_F}{L}\right\} \quad (18a)$$

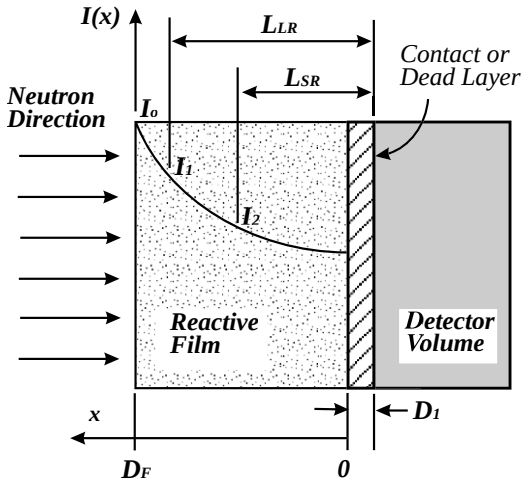

Fig. 14. Coordinate system for front irradiation of coated neutron detectors.

for $D_F \leqslant L$, and

$$S_p(D_F) = \frac{F_p e^{-\Sigma_F(D_F-L)}}{4\pi I_0}\int_0^L I_0 2\pi\Sigma_F e^{-\Sigma_F(D_F-x)}\left(1-\frac{x}{L}\right)dx$$
$$= 0.5F_p e^{-\Sigma_F(D_F-L)}\left\{\left(1+\frac{1}{\Sigma_F L}\right)\times(1-e^{-\Sigma_F L})-1\right\} \quad (18b)$$

for $D_F > L$, where F_p refers to the branching ratio of the reaction product emission. The total sensitivity can be found by adding all of the reaction product sensitivities, hence

$$S(D_F)|_{Total} = \sum_{p=1}^{N} S_p(D_F) \quad (19)$$

where N is the number of different possible reaction products. In the case of ^{10}B-based films N equals 4, whereas for ^{6}Li-based films N equals 2. Note from Eq. (18b) that the value of S_p decreases as D_F becomes larger than the value of L. As a result, there will be an optimal neutron reactive film thickness for front irradiated detectors. Since the minimum particle detection threshold determines the average effective range (L), the optimal film thickness is also a function of the LLD setting.

The maximum neutron sensitivity contribution from any particular charged-particle reaction product can found by differentiating Eq. (18a) with respect to the film thickness D_F,

$$\frac{dS_p}{dD_F} = \frac{d}{dD_F}\left[0.5F_p\left\{\left(1+\frac{1}{\Sigma_F L}\right)(1-e^{-\Sigma_F D_F})-\frac{D_F}{L}\right\}\right]$$
$$= 0.5F_p\left\{\left(\Sigma_F+\frac{1}{L}\right)e^{-\Sigma_F D_F}-\frac{1}{L}\right\} \quad (20)$$

where the local maxima is found by setting Eq. (20) to zero. For a particular charged-particle reaction product p, the film thickness that allows for the maximum detection efficiency is

$$D_F|_{P_{max}} = \frac{1}{\Sigma_F}\ln(\Sigma_F L+1). \quad (21)$$

Fig. 15 shows the value of $D_{F(p_{max})}$ as a function of the $\Sigma_F L$ product. As shown, at small values of $\Sigma_F L$, the value of $D_{F(p_{max})}$ is approximately equal to the value of L. When all reaction products are included, the optimal film thickness is determined by taking the derivative of Eq. (19). The process becomes complicated by the need to select the appropriate equation, either Eq. (18a) or Eq. (18b), for each of the reaction products. For the sake of illustrating the behavior of the system, some appropriate assumptions can be made. In a two-product system, the long-range particle can be assumed to dominate. Hence, the derivative of Eq. (18a) is used for the long-range particle and

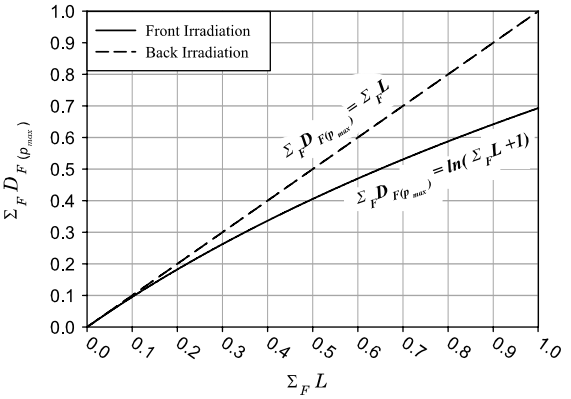

Fig. 15. The individual particle optimized thickness $D_{F(p_{max})}$ as a function of the $\Sigma_F L$ product, showing that $D_{F(p_{max})} < L$ for front irradiation of detectors coated with high $\Sigma_F L$ value films. For back irradiation, $D_{F(p_{max})}$ and L are equal.

the derivative of Eq. (18b) is used for the short-range particle. Continuing with such a theme, for multiple particle systems (as with $^{10}B(n,\alpha)^{7}Li$), we use Eq. (18a) for the longest-range particle, and Eq. (18b) for the remaining particles. It can, therefore, be shown that

$$D_F|_{max} = \frac{1}{\Sigma_F} \ln\left[(\Sigma_F L_{LR} + 1) - \frac{L_{LR}}{F_{LR}} \sum_{p=2}^{N} \Psi_p\right] \quad (22)$$

where the subscript LR refers to the longest-range reaction product, N is the total number of different reaction products, and

$$\Psi_p = F_p \Sigma_F e^{\Sigma_F L_p} \times \left[\left(1 + \frac{1}{\Sigma_F L_p}\right)(1 - e^{-\Sigma_F L_p}) - 1\right] \quad (23)$$

which represents the remaining shorter range charged-particle reaction products. For a two-particle system in which the reaction products differ in mass, Eqs. (22) and (23) are reliable. However, with a multiple-particle system, the reaction product branching ratios may dictate that a shorter-range particle dominates the maximum achievable sensitivity, in which case Eq. (22) must be altered to properly represent the condition. In such cases, the optimal film thickness can be found by iteratively solving Eq. (19) for the maximum calculated efficiency and corresponding film thickness. Regardless, the ΣL product remains an important parameter in determining the optimum neutron reactive film thickness.

It is important to note from Fig. 14 that, for front side irradiation, the highest neutron interaction rate within the film is the furthest film distance from the film–detector junction. Additionally, the lowest neutron flux and corresponding interaction rate is adjacent to the film–detector junction, and the rate decreases as the film thickness increases.

Overall, the front-coated device operates only as a neutron *counter*. In order to discriminate against background gamma rays, the energy discriminator should be set high enough to reduce the probability of mistaking a gamma ray event for a neutron event. Figs. 16 and 17 show the expected thermal neutron detection efficiency for ^{10}B, ^{6}LiF, and ^{6}Li films as a function of thickness (D_F) with an LLD setting of 300 keV. The ^{10}B film has the lowest efficiency, peaking at approximately 4% detection efficiency. However, the ^{10}B film thickness required to achieve 4% efficiency is only 2.4 μm, whereas comparable efficiencies for pure ^{6}Li and ^{6}LiF layers require 12 and 18 μm of material, respectively. Only a marginal gain in efficiency can be achieved with ^{6}LiF, peaking at approximately 4.4% thermal neutron detection efficiency at a film thickness of 26 μm. Pure ^{6}Li offers the highest achievable efficiency, peaking at 11.5% efficiency for a film thickness of 100 μm. Although pure ^{6}Li may appear attractive as a relatively efficient thermal neutron detection film, the fabrication, handling, and packaging issues render detector production much more difficult

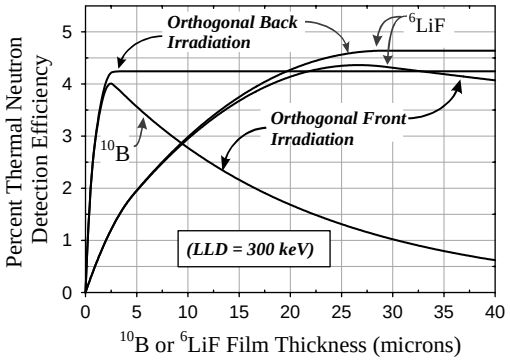

Fig. 16. The calculated thermal neutron detection efficiencies for front and back irradiation as a function of film thickness for ^{10}B- and ^{6}LiF-coated detectors.

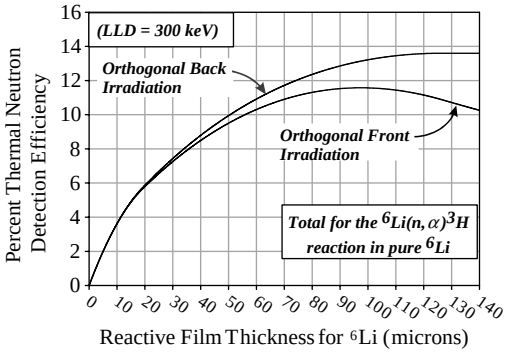

Fig. 17. The calculated thermal neutron detection efficiencies for front and back irradiation as a function of film thickness for pure ^{6}Li-coated detectors.

than that required for ^{10}B or ^{6}LiF-coated devices. Additionally, other detector configurations can increase the efficiency of ^{10}B- or ^{6}LiF- coated devices.

4.3. Backside irradiation

To eliminate the dependence of the optimum film thickness on the LLD setting, the thin-film-coated neutron detector can be designed to operate via backside irradiation. The geometry of such a device is depicted in Fig. 18. Note that neutron absorption can take place in the detector before reaching the reactive film, and these losses must be accounted for by incorporating Eq. (3) for each layer. Hence, the neutron intensity reaching the reactive film can be represented by

$$I|_{\text{interface}} = I_0 \prod_{i=1}^{M} e^{-\Sigma_i D_i} \tag{24}$$

where Σ_i is the macroscopic cross-section for each layer, D_i is the thickness of each layer, and M is the number of detector layers *excluding* the thermal neutron reactive film. Assuming orthogonal backside irradiation, the sensitivity contribution for each particle is determined by integrating the product of Eqs. (5) and (6) over the film thickness D_F. Hence, the sensitivity is

$$\begin{aligned} S_p(D_F) &= \frac{F_p}{4\pi I_0} I_0 \prod_{i=1}^{M} e^{-\Sigma_i D_i} \\ &\quad \times \int_0^{D_F} 2\pi \Sigma_F e^{-x\Sigma_F} \left(1 - \frac{x}{L}\right) dx \\ &= 0.5 F_p \prod_{i=1}^{M} e^{-\Sigma_i D_i} \\ &\quad \times \left\{ \left(1 - \frac{1}{\Sigma_F L}\right)(1 - e^{-\Sigma_F D_F}) + \frac{D_F}{L} e^{-\Sigma_F D_F} \right\}, \\ &\text{for } D_F \leqslant L \end{aligned} \tag{25a}$$

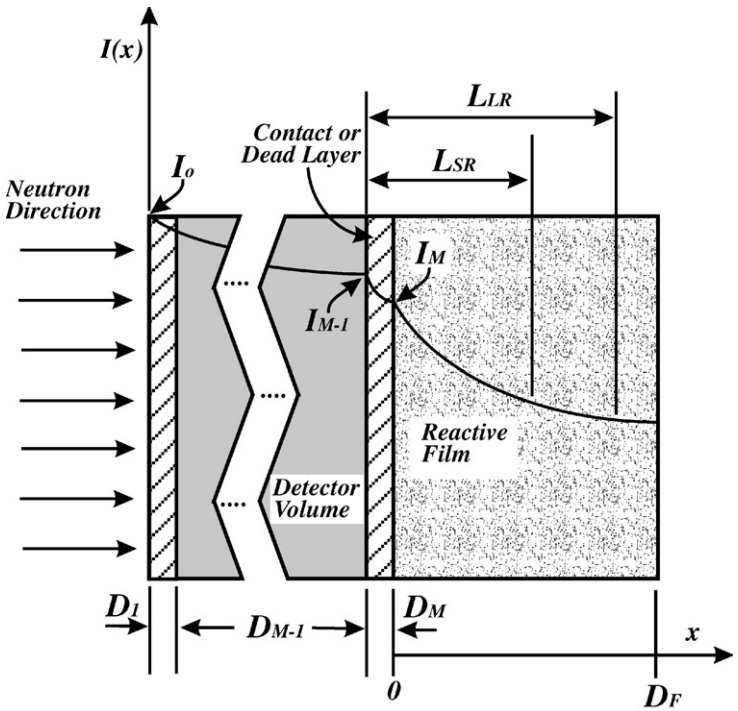

Fig. 18. Coordinate system for back irradiation of coated neutron detectors.

and

$$S_p(D_F) = \frac{F_p}{4\pi I_0} I_0 \prod_{i=1}^{M} e^{-\Sigma_i D_i} \times \int_0^L 2\pi\Sigma_F e^{-x\Sigma_F}\left(1-\frac{x}{L}\right) dx$$
$$= 0.5F_p \prod_{i=1}^{M} e^{-\Sigma_i D_i} \times \left\{\left(1-\frac{1}{\Sigma_F L}\right)(1-e^{-\Sigma_F L}) + e^{-\Sigma_F L}\right\},$$
$$\text{for } D_F > L. \quad (25b)$$

Contrary to the front irradiation case, the lowest neutron interaction rate within the reactive film is the furthest film distance from the film–detector junction, and the highest neutron interaction rate within the reactive film is adjacent to the film–detector junction (Fig. 18). As a result, the backside-irradiated devices can achieve slightly higher neutron detection efficiencies than front side irradiated devices (Figs. 16 and 17). To use the backside irradiation arrangement effectively, the semiconductor detector layers should be very thin and composed of materials with relatively small neutron interaction cross-sections. Otherwise, significant neutron losses will occur before they can reach the reactive film, thereby undermining the advantage of backside irradiation. The total neutron sensitivity can be found by employing Eqs. (19) and (25). It can also be shown by differentiating Eq. (25a) and solving for the local maxima, as was done with Eq. (18a), that $D_{F(p_{max})}$ for backside irradiation is equal to L (see Fig. 15).

4.4. Detector angle and the effects

4.4.1. The simple infinite plane case

Turning the device at an angle is a method that can be used to increase the thermal neutron detection efficiency per unit area for neutrons approaching from one direction. In the present analysis, it is assumed that the device has infinite dimensions in the Z (perpendicular to the page) and Y directions, thereby eliminating end effects. Referring to Fig. 19, the device can be rotated through angle θ between 0° and 90° with respect to the direction of the intersecting neutrons, where a detector at 0° is orthogonal to the neutron beam and 90° is parallel to the neutron beam.

The effective neutron absorbing film thickness is increased with increasing angle, while the charged-particle transit distance required to reach the detector interface remains unchanged. In other words, the neutron absorption efficiency of the detector is increased while maintaining the same minimum detectable solid angle. The neutron detection efficiency for each charged-particle reaction product is represented by

$$S_p(D_F) = 0.5F_p\left\{\left(1+\frac{\cos\theta}{\Sigma_F L}\right)(1-e^{-\Sigma_F D_F/\cos\theta}) - \frac{D_F}{L}\right\}$$
$$\text{for } D_F \leqslant L \quad (26a)$$

and

$$S_p(D_F) = 0.5F_p e^{-\Sigma_F(D_F-L)/\cos\theta} \times \left\{\left(1+\frac{\cos\theta}{\Sigma_F L}\right)(1-e^{-\Sigma_F L/\cos\theta}) - 1\right\}$$
$$\text{for } D_F > L. \quad (26b)$$

With the LLD set at 300 keV and $D = L_{LR}$, Fig. 20 shows a comparison of the calculated sensitivities for a ^{10}B-coated device as a function of angle. Notice how the efficiency increases dramatically at angles greater than 45°. The results would indicate that turning the device such that the intersection angle is almost 90° would allow for very high efficiencies, yet the result is a consequence of the infinite plane assumption. For small devices, the actual neutron detection efficiency will be significantly less due to both the "effective sensitive area" decreasing in size and charged particle end effect losses.

4.4.2. The short plane case

The effective sensitive area (A_{eff}) pertains to the actual projected area that the neutron beam intersects for a given device angle. For the single-side-coated neutron detection device, A_{eff} changes proportionally to $\cos\theta$, or rather

$$A_{eff} = A|_{\theta=0}\cos\theta + R_\perp D_F \sin\theta \quad (27)$$

where $R_\perp$ is the converter length parallel to the axis of rotation (see Fig. 19). Since D_F is relatively thin, the actual sensitivity will decrease almost to zero as

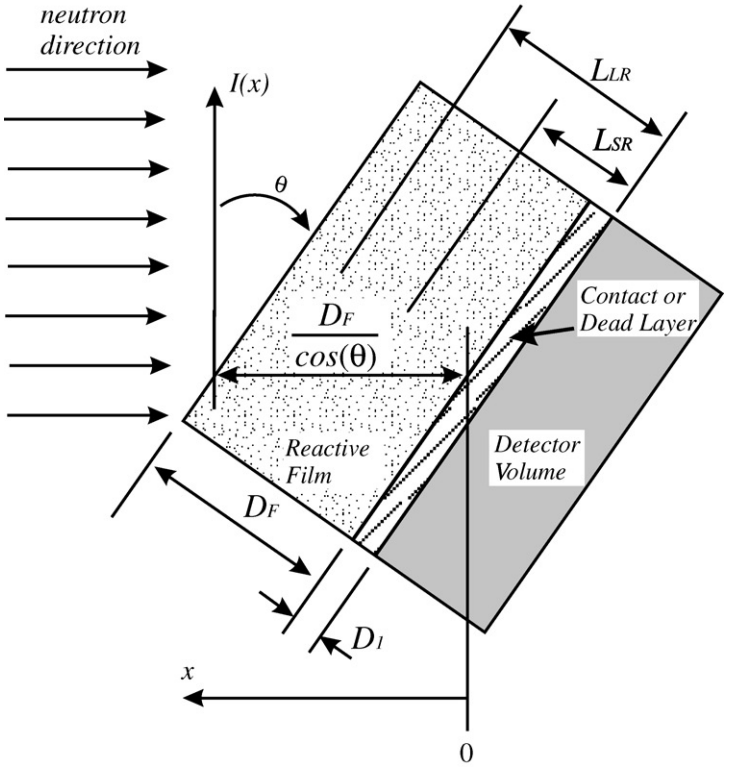

Fig. 19. The coordinate system used for determining angular effects on neutron detection efficiency.

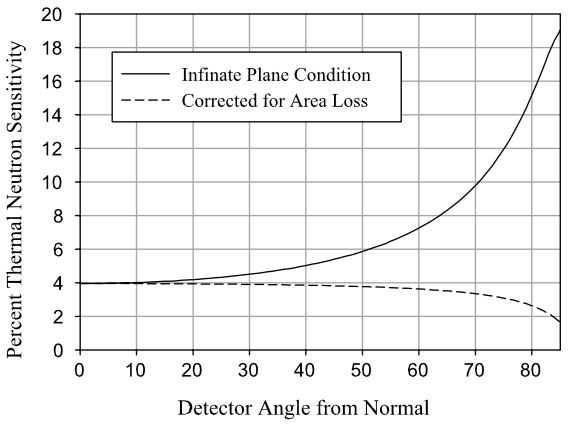

Fig. 20. Although the infinite plane treatment appears to show efficiency as a strongly changing function with angle, in reality the thermal neutron detection efficiency is fairly constant for angles up to 60°. Efficiency diminishes at source to detector angles greater than 60°.

the device angle increases to 90°. Correcting for the diminishing apparent detector area, the corrected neutron detection efficiency is represented by

$$S_p(D_F) = 0.5\cos\theta\, F_p \times \left\{\left(1+\frac{\cos\theta}{\Sigma_F L}\right)(1-e^{-\Sigma_F D_F/\cos\theta}) - \frac{D_F}{L}\right\} \quad \text{for } D_F \leqslant L. \tag{28a}$$

and

$$S_p(D_F) = 0.5\cos\theta\, F_p e^{-\Sigma_F(D_F-L)/\cos\theta} \times \left\{\left(1+\frac{\cos\theta}{\Sigma_F L}\right)(1-e^{-\Sigma_F L/\cos\theta}) - 1\right\} \quad \text{for } D_F > L. \tag{28b}$$

The results are shown in Fig. 20, in which it is clear that the efficiency actually does not increase, but diminishes at angles above 60°. The very

important result also indicates that the sensitivity of thin film coated detectors is largely unchanged over a large angular distribution, remaining almost constant for neutron sources at angles 60° or less from normal to the detector front and back planes.

4.5. Efficiency as a function of LLD criteria

Thus far a 300 keV minimum detectable energy criteria has been imposed such that the LLD is set at 300 keV equivalent. As the case may be, the background radiation field, most likely gamma rays, will either allow for a higher or lower LLD setting. The observed efficiency for front or back irradiation devices will increase as the LLD is lowered, and will decrease as the LLD is raised. Obviously, if the LLD is lowered, then the minimum detectable energy criteria is less, which allows for longer effective ranges for both particles. Longer effective ranges result in larger ΣL products (see Tables 1 and 2) and allow for thicker films; hence the neutron detection efficiency should increase. The opposite effect is true if the LLD is raised.

Since the effective range (L) is a function of the LLD setting, then the optimum film thickness will also change as a function of LLD setting. Using the L and ΣL values listed in Tables 1 and 2, Fig. 21 shows the expected efficiencies for ^{10}B-coated devices as a function of LLD setting for front irradiation. As can be seen, simply reducing the LLD to lower values can increase the efficiency, yet the risk of including background radiation events, as from gamma rays, increases as the LLD is lowered [20]. Hence, the operator must find a useful balance for the environment. Also, it is important to note from Fig. 21 that the optimal film thickness changes as a function of LLD as well. Prior knowledge of the radiation environment will assist in design the optimum film thickness for the device.

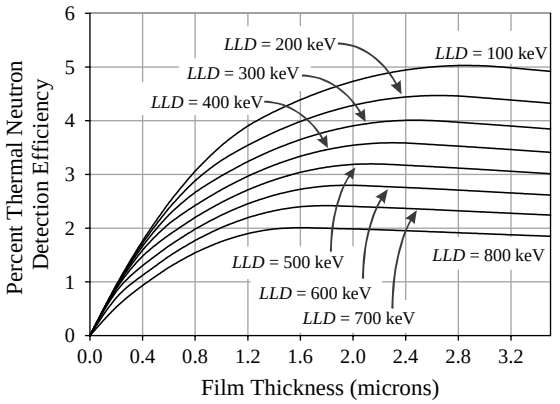

Fig. 21. Thermal neutron detection efficiency as a function of ^{10}B thickness and LLD setting.

5. Advanced designs

5.1. Stacked detectors

Stacking individual devices can increase the overall system neutron detection efficiency, although the increase in efficiency does not accumulate linearly. The initial neutron flux will be attenuated by each of the neutron absorbing layers. As a result, the neutron flux decreases for each subsequent detector and the effect must be taken into account when calculating the overall neutron detection efficiency of the stack. For the case in which the neutron sensitive film is of the same thickness for all detectors in the stack, the total sensitivity to a reaction product particle type can be expressed as

$$S_p(D_F) = 0.5F_p \sum_{n=0}^{N-1} \left\{ e^{-n(\Sigma_F D_F)} \prod_{i=1}^{M} e^{-n(\Sigma_i D_i)} \right\} \times \left\{ \left(1 + \frac{1}{\Sigma_F L}\right)(1 - e^{-\Sigma_F D_F}) - \frac{D_F}{L} \right\} \quad \text{for } D_F \leqslant L \tag{29a}$$

and

$$S_p(D_F) = 0.5F_p e^{-\Sigma_F(D_F - L)} \sum_{n=0}^{N-1} \left\{ e^{-n(\Sigma_F D_F)} \prod_{i=1}^{M} e^{-n(\Sigma_i D_i)} \right\} \times \left\{ \left(1 + \frac{1}{\Sigma_F L}\right)(1 - e^{-\Sigma_F L}) - 1 \right\} \quad \text{for } D_F > L \tag{29b}$$

where N is the number of detectors in the stack, M is the number of layers in each of the individual detectors *excluding* the neutron reactive film, n is

the detector number, and i is the film number. For the case in which there is only one detector, the reader may verify that Eqs. (29a) and (29b) reduce to Eqs. (18a) and (18b), respectively.

The authors first consider the case in which the semiconductor substrate has negligible neutron scattering and absorption. The optimum thickness for the individual neutron reactive films decreases as the number of detectors in the stack increases. Figs. 22–24 show the calculated thermal neutron detection efficiencies for pure ^{10}B, ^{6}LiF, and pure ^{6}Li as a function of film thickness and the number of detectors in the stack. Only slight differences in efficiency are detectable for the ^{10}B and ^{6}LiF coated devices as shown in Figs. 22 and 23. The calculations indicate that a stack of ^{6}LiF coated devices can achieve slightly higher efficiency than a stack of ^{10}B coated devices for a small number of detectors, whereas a stack of ^{10}B coated devices can achieve a slightly higher efficiency than a stack of ^{6}LiF coated devices for a relatively large number of detectors. Yet, the optimum thickness of material required in the ^{6}LiF film is over 10 times greater than that required of the ^{10}B film, indicating that detector fabrication will be easiest for ^{10}B-coated devices. Fig. 24 shows the calculated thermal neutron detection efficiency for a stack of ^{6}Li-coated devices, in which it becomes clear that a stack of ^{6}Li-coated devices provides much higher achievable neutron detection efficiencies than stacks of ^{10}B-coated or ^{6}LiF-coated devices. However, the hygroscopic and reactive nature of pure ^{6}Li requires special handling and processing techniques in order to achieve an accurate and optimized film thickness.

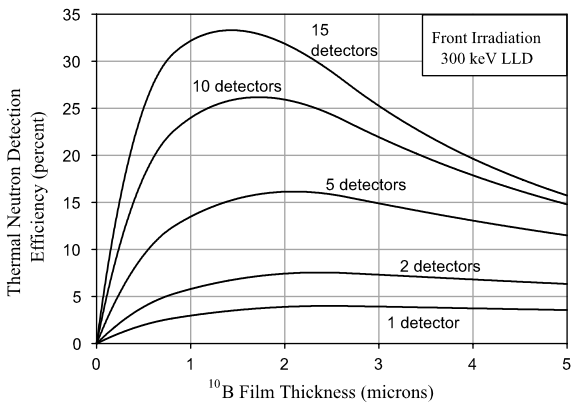

Fig. 22. Thermal neutron detection efficiency as a function of ^{10}B thickness and number of stacked detectors.

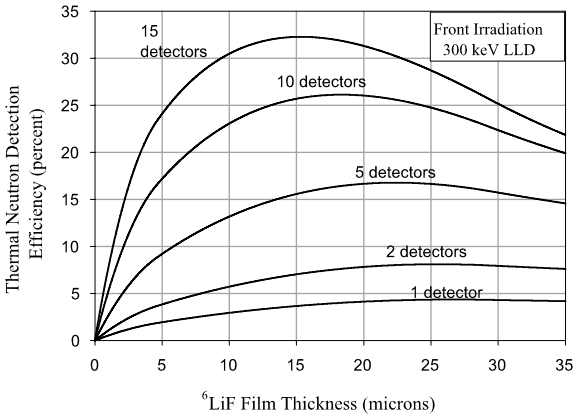

Fig. 23. Thermal neutron detection efficiency as a function of ^{6}LiF thickness and number of stacked detectors.

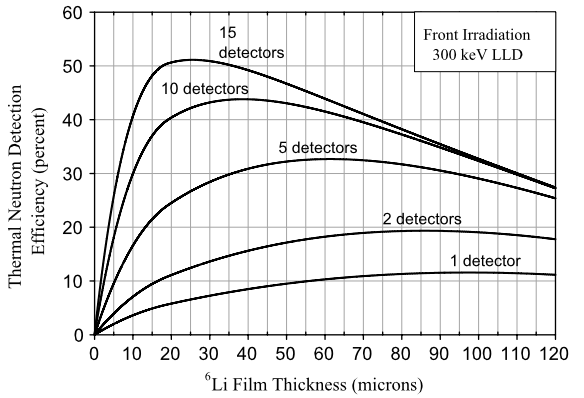

Fig. 24. Thermal neutron detection efficiency as a function of ^{6}Li thickness and number of stacked detectors.

In all cases shown in Figs. 22–24, the optimum film thickness decreases as the number of detectors in the stack increases. Additionally, the change in efficiency as a function of film thickness increases as the number of detectors in the stack increases. Hence, film thickness accuracy becomes increasingly important as the stack number increases.

It should also be pointed out that the *increase* in efficiency per added detector diminishes as the number of detectors in the stack increases. The overall device design should incorporate a

reasonable number of detectors compatible with the available detector power supply and output electronics. Additionally, increasing devices in the detector stack will also increase the system electronic noise, thereby placing an additional requirement upon the system LLD setting.

Operation of the detector stack affects other aspects of the performance as well. Two straightforward methods of applying voltage across the detector stack and extracting the signal are the parallel method and the series method. Briefly explained, detectors operated in parallel are individually biased with one electrode connected to the pre-amplifier circuit. Detectors operated in series have the bias applied across the entire detector stack, which are connected in series, and only one of the devices in the series is connected to the pre-amplifier circuit. The parallel method allows for retention of the total induced charge signal, but the system capacitance increases by the number of detectors in the stack. The series method reduces the system capacitance, but the induced charge output signal is divisively diminished by the number of detectors in the stack, thereby producing a weaker electronic output pulse.

5.2. Double-coated designs

A method of increasing the overall efficiency of a device incorporates a double-layered film, such as with ^{6}LiF on ^{10}B or ^{6}Li on ^{10}B. From Tables 1 and 2, it is clear that the ^{10}B(n,α)^{7}Li reaction products have shorter ranges within ^{10}B material than do ^{6}Li(n,α)^{3}H reaction products. Hence, it is possible to apply a coating of ^{10}B followed by a coating of either ^{6}LiF or ^{6}Li (as shown in Fig. 25). The charged-particle reaction products emanating from ^{10}B(n,α)^{7}Li reactions can reach the detector as before since the film is applied directly to the detector contact. In addition, the longer range charged particle products emanating from ^{6}Li(n,α)^{3}H reactions can also still reach the detector even though they must transit the ^{10}B film as well. Since the ^{10}B film has a higher neutron interaction cross-section than ^{6}LiF or ^{6}Li films, a net gain is realized. Hence, the short-product-range and high-cross-section material is deposited closest to the contact (denoted converter 1) while the long-range and low-cross-section material is placed atop the first film where the upper film is denoted converter 2. The opposite case renders no improvement, and in fact actually decreases efficiency.

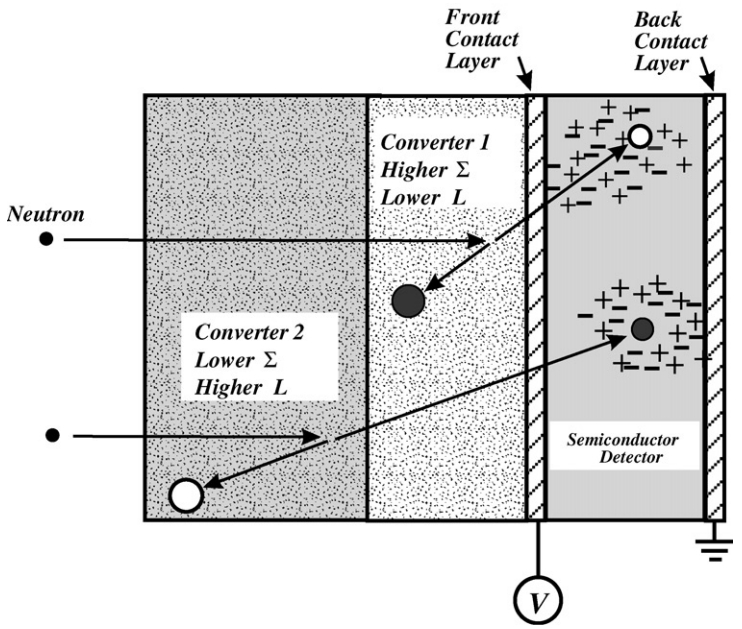

Fig. 25. The general concept of a "double-coated" design.

Table 3
Corrected $^{6}Li(n,\alpha)^{3}H$ reaction product ranges for both ^{6}LiF films on ^{10}B and ^{6}Li Films on ^{10}B. The minimum detection threshold used for the calculation was 300 keV

^{10}B thickness (μm)	^{6}LiF atop ^{10}B		^{6}Li atop ^{10}B	
	2.730 MeV Triton $L_{D_{F1},D_{F2}}$ (μm)	2.050 MeV α-particle $L_{D_{F1},D_{F2}}$ (μm)	2.730 MeV Triton $L_{D_{F1},D_{F2}}$ (μm)	2.050 MeV α-particle $L_{D_{F1},D_{F2}}$ (μm)
0.0	29.2	4.65	127	19.1
0.5	29.1	4.57	126	17.0
1.0	29.0	4.43	124	15.4
1.5	28.9	4.35	122	13.7
2.0	28.8	4.34	120	12.0
2.5	28.8	4.30	118	10.3
3.0	28.8	4.25	116	8.40
3.5	28.8	4.23	113	6.80
4.0	28.8	4.23	112	5.0

Calculating the actual efficiency of the double film as a function of both film depths can be a bit complicated since the particle ranges and energy losses are not linearly coupled. Additionally, the effective range changes as a function of angle since the distance that the charged-particle reaction product must traverse converter 1 becomes a function of $D_{F1}\sec\theta$, where D_{F1} is the thickness of converter 1 and θ refers to the angle increasing from orthogonal. Hence, Monte-Carlo simulations can be used for the best results. However, given the thin applications of ^{10}B that are of practical use (0 to 2.5 μm), it is fortuitous to note that the maximum range, with a 300 keV LLD equivalent for 2.7 MeV tritons and 2.05 MeV alpha particles, is only slightly different between that of a pure ^{6}LiF film and a layered film of ^{6}LiF and 2.5 μm of ^{10}B [32]. Therefore, sufficiently accurate results can be acquired by using an average effective range for the $^{6}Li(n,\alpha)^{3}H$ reaction products, which is only slightly different than for the pure ^{6}LiF film. Unfortunately, the effective range *does* change considerably for a system with a pure ^{6}Li film atop a ^{10}B film. As a result, the actual effective range, rather than an average, should be used when determining the optimum film thickness combination. Table 3 shows the calculated maximum ranges (300 keV equivalent) for the $^{6}Li(n,\alpha)^{3}H$ reaction products for both pure ^{6}Li films and ^{6}LiF films on various depths of ^{10}B films.

For frontal irradiation, the efficiency for converter 1 is similar to Eqs. (18a) and (18b), with the difference noted as being corrected for neutron attenuation through converter 2:

$$\begin{aligned} S_p(D_{F1}) &= \frac{F_p}{4\pi I_0} e^{-\Sigma_{F2}D_{F2}} \\ &\quad \times \int_0^{D_{F1}} I_0 2\pi\Sigma_{F1} e^{-\Sigma_{F1}(D_{F1}-x)}\left(1-\frac{x}{L_{F1}}\right)dx \\ &= 0.5F_p e^{-\Sigma_{F2}D_{F2}} \\ &\quad \times \left\{\left(1+\frac{1}{\Sigma_{F1}L_{F1}}\right)(1-e^{-\Sigma_{F1}D_{F1}}) - \frac{D_{F1}}{L_{F1}}\right\} \end{aligned} \tag{30a}$$

for $D_{F1} \leqslant L_{F1}$, and

$$\begin{aligned} &S_p(D_{F1}) \\ &= \frac{F_p e^{-\Sigma_{F1}(D_{F1}-L_{F1})}}{4\pi I_0} e^{-\Sigma_{F2}D_{F2}} \\ &\quad \times \int_0^{L_{F1}} I_0 2\pi\Sigma_{F1} e^{-\Sigma_{F1}(D_{F1}-x)}\left(1-\frac{x}{L_{F1}}\right)dx \\ &= 0.5F_p e^{-\Sigma_{F2}D_{F2}} e^{-\Sigma_{F1}(D_{F1}-L_{F1})} \\ &\quad \times \left\{\left(1+\frac{1}{\Sigma_{F1}L_{F1}}\right)(1-e^{-\Sigma_{F1}L_{F1}}) - 1\right\} \end{aligned} \tag{30b}$$

for $D_{F1} > L_{F1}$, where the argument $\Sigma_{F2}D_{F2}$ accounts for neutron absorption in converter 2 before they reach converter 1. Note that the effective range is not altered since the products produced need only transit through converter 1 to reach the detector interface. The efficiency contribution from converter 2 must account for the change in effective range for reaction products as

they transit from converter 2 into converter 1, and it must account for the reduction in the maximum solid angle detector intersection probability that is diminished by converter 1. The efficiency contribution from converter 2 is:

$$
\begin{aligned}
&S_p(D_{F2}) \\
&= \frac{F_p}{4\pi I_0}\int_{D_{F1}}^{D_{F2}+D_{F1}} I_0 2\pi\Sigma_{F2} e^{-\Sigma_{F2}(D_{F2}-x)} \\
&\quad\times\left(1-\frac{x}{L_{D_{F1},D_{F2}}}\right)dx \\
&= \frac{0.5F_p}{\Sigma_{F2}L_{D_{F1},D_{F2}}} \\
&\quad\times\left\{\left(1+\Sigma_{F2}L_{D_{F1},D_{F2}}-\Sigma_{F2}[D_{F1}+D_{F2}]\right)\right. \\
&\quad-(1+\Sigma_{F2}L_{D_{F1},D_{F2}}-\Sigma_{F2}D_{F1}) \\
&\quad\left.\times(e^{\Sigma_{F2}(D_{F1}-D_{F2})})\right\} \qquad (31a)
\end{aligned}
$$

for $D_{F2}+D_{F1}\leqslant L_{D_{F1},D_{F2}}$ and

$$
\begin{aligned}
&S_p(D_{F2}) = \frac{F_p e^{-\Sigma_{F2}(D_{F2}-L_{D_{F1},D_{F2}})}}{4\pi I_0} \\
&\times\int_{D_{F1}}^{L_{D_{F1},D_{F2}}} I_0 2\pi\Sigma_{F2} e^{-\Sigma_{F2}(D_{F2}-x)}\left(1-\frac{x}{L_{D_{F1},D_{F2}}}\right)dx \\
&= \frac{0.5F_p e^{-\Sigma_{F2}(D_{F2}-L_{D_{F1},D_{F2}})}}{\Sigma_{F2}L_{D_{F1},D_{F2}}}\left\{e^{\Sigma_{F2}(L_{D_{F1},D_{F2}}-[D_{F2}+D_{F1}])}\right. \\
&-(1+\Sigma_{F2}L_{D_{F1},D_{F2}}-D_{F1}\Sigma_{F2})e^{\Sigma_{F2}(D_{F1}-D_{F2})}\} \qquad (31b)
\end{aligned}
$$

for $D_{F2}+D_{F1} > L_{D_{F1},D_{F2}}$, where $L_{D_{F1},D_{F2}}$ represents the average effective range for the layered film (see Table 3).

From Eq. (30) through 31, the thermal neutron detection efficiencies as a function of film thickness are shown in Figs. 26–29. Figs. 26 and 27 show the expected results from a ^{6}LiF/^{10}B system and Figs. 28 and 29 show the expected results from a ^{6}Li/^{10}B system, showing an optimum efficiency of 6.8% for the former and 12.86% for the latter.

5.3. The sandwich design

"Sandwich" designs can assist in increasing the overall thermal neutron detection efficiency by either doubling the amount of neutron reactive material or doubling the sensitive region in contact with the neutron reactive material. Two configurations will be discussed in the following section; the double-sided film detector design and the double-inward facing detector design.

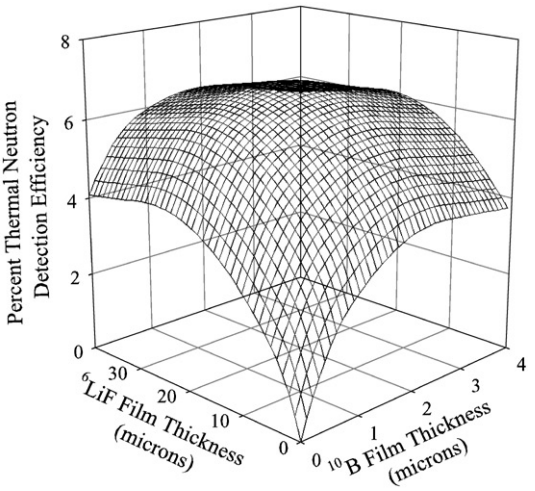

Fig. 26. The thermal neutron detection efficiency for a double-coated detector using ^{6}LiF atop ^{10}B.

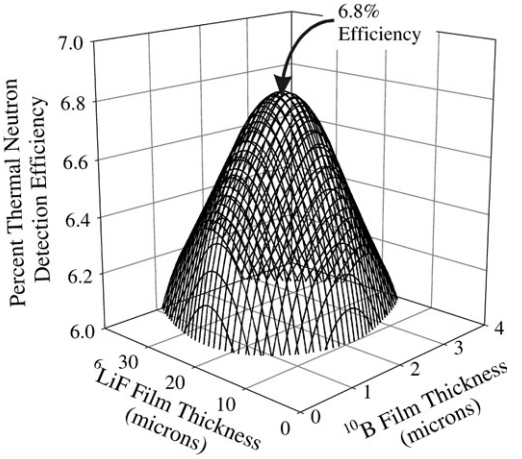

Fig. 27. Expanded view of ^{6}LiF atop a ^{10}B film, showing the optimized thermal neutron detection efficiency is 6.8% when a 300 keV LLD criteria is used.

5.3.1. Double-sided film (or outward-facing) detector

The double-sided film detector consists of a semiconductor detector in which a neutron sensitive film is deposited on the front and backsides. The advantages include high neutron detection efficiency and a very low probability of reaction

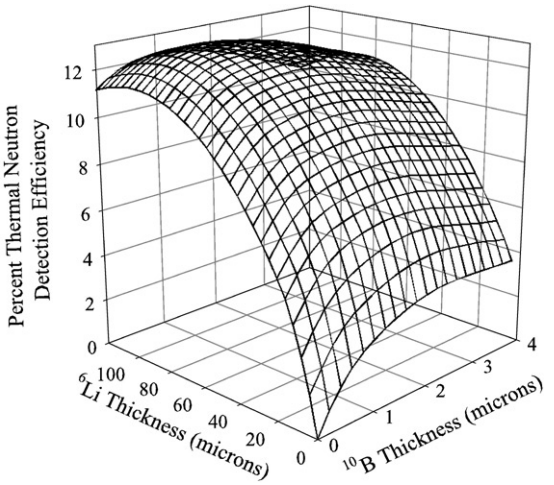

Fig. 28. The thermal neutron detection efficiency for a double-coated detector using ^{6}Li atop ^{10}B.

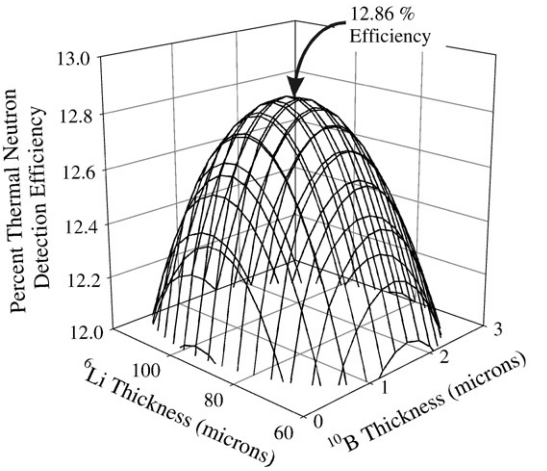

Fig. 29. Expanded view of ^{6}Li atop a ^{10}B film, showing the optimized thermal neutron detection efficiency is 12.86% when a 300 keV LLD criteria is used.

product coincidence counts (from a single neutron) during a measurement. Disadvantages include higher operating voltages and higher gamma ray background interference.

Fig. 30 shows a simple depiction of the double-sided film detector design, in which neutron reactive films are deposited on both sides of the device. Semiconductor diodes rarely have similar contacts for both surfaces and the analysis should take this point into account. In general, neutrons orthogonally intersecting the front of the device undergo some absorption in the first film, experience further losses in the detector contacts and detector bulk, and again undergo absorption in the second film. Charged particles emitted from reactions in either film can be detected from the detector side adjacent to the film. For simplicity, assume that the neutron reactive films, both front and back, are of the same thickness.

Consider the case in which the detector thickness is greater than L_{LR}. The solution to the overall efficiency can be found by adding the appropriate mix of Eqs. (18) and (25), while accounting for neutron attenuation in the first film. Hence, for each charged-particle reaction product,

$$S_p(D_F) = 0.5F_p\left[\left\{\left(1+\frac{1}{\Sigma_F L}\right)(1-e^{-\Sigma_F D_F}) - \frac{D_F}{L}\right\} + e^{-\Sigma_F D_F}\prod_{i=1}^{M} e^{-\Sigma_i D_i}\left\{\left(1-\frac{1}{\Sigma_F L}\right) \times (1-e^{-\Sigma_F D_F}) + \frac{D_F}{L}e^{-\Sigma_F D_F}\right\}\right], \quad D_F \leqslant L \tag{32a}$$

and

$$S_p(D_F) = 0.5F_p\left[e^{-\Sigma_F(D_F-L)} \times \left\{\left(1+\frac{1}{\Sigma_F L}\right)(1-e^{-\Sigma_F L}) - 1\right\} + e^{-\Sigma_F D_F}\prod_{i=1}^{M} e^{-\Sigma_i D_i} \times \left\{\left(1-\frac{1}{\Sigma_F L}\right)(1-e^{-\Sigma_F L}) + e^{-\Sigma_F L}\right\}\right], \quad D_F > L \tag{32b}$$

where the subscript i refers to the bulk detector layer and the contact layers, both front and back, and M refers to the total number of layers *excluding* the neutron reactive films. Note that the back facing film terms (second portion) in Eqs. (32a) and (32b) are corrected for neutron attenuation through the front facing neutron reactive film.

The device will only work properly if the applied operating voltage extends the electric field entirely across the semiconductor detector. The entire detector bulk then becomes sensitive to charge

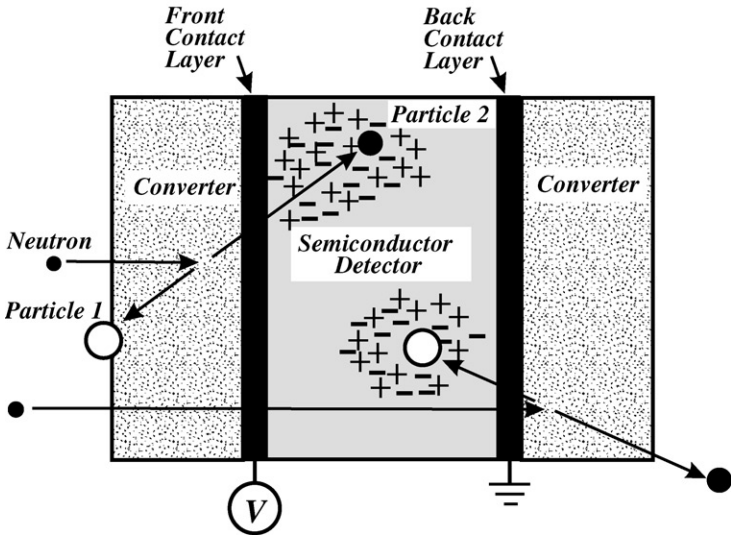

Fig. 30. The most basic "sandwich" design, in which a neutron reactive coating is placed upon both sides of a diode.

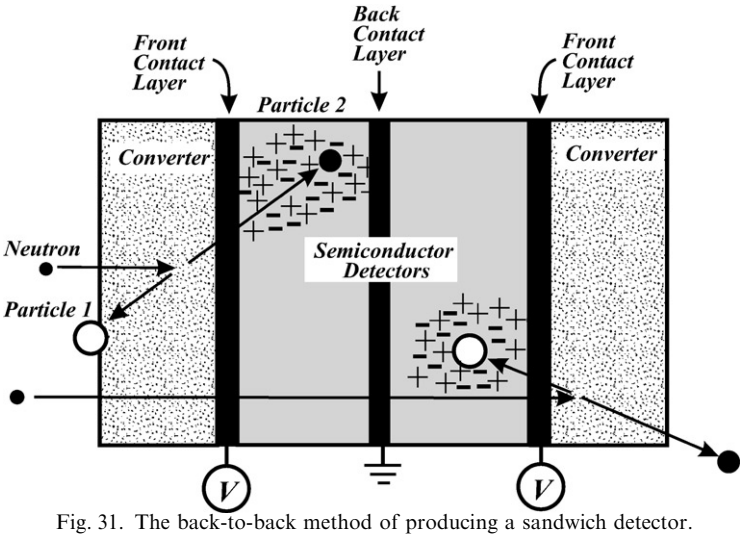

Fig. 31. The back-to-back method of producing a sandwich detector.

particles entering the device from either side. Unfortunately, it also becomes more sensitive to background gamma rays as well. Minimizing the bulk detector thickness minimizes the required operating voltage and reduces background radiation noise. However, decreasing the overall bulk detector thickness increases the device capacitance, which produces higher electronic noise. Materials composed of relatively high atomic number (Z) materials increase the gamma ray absorption probability. Hence, a low Z material is preferred to reduce gamma ray background interference.

An alternative, but similar, method of producing the same effect is shown in Fig. 31, in which two single coated devices are placed back-to-back and connected as if they were one device. The advantages includes:

- Simple fabrication with only one coating step.

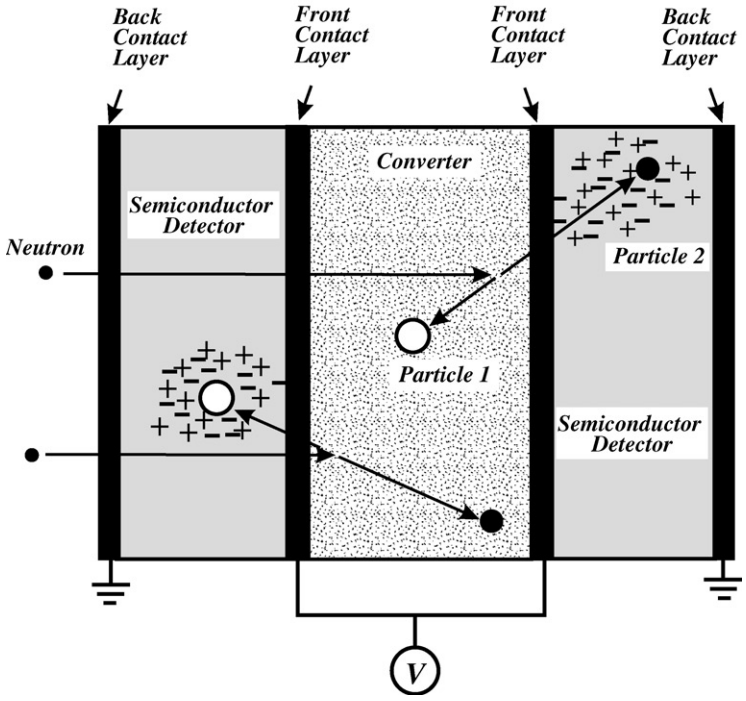

Fig. 32. The double-inward facing detector design.

- Lower operating voltages, requiring only that needed to deplete a small region near the reactive film.

The main disadvantage is the increase in capacitance, which will double when using two identical devices.

5.3.2. *Double-inward facing detectors*

Another design that does not rely on the full depletion of the detectors, and can still be operated with modest operating voltages, is the double-inward facing detector design, as shown in Fig. 32. The design offers another method to increase the thermal neutron detection efficiency, but does have drawbacks.

If the neutron reactive film thickness is too thin, coincident charged particle emissions from a single neutron absorption event can be measured simultaneously by both detectors, thus giving rise to the erroneous recording of two neutron interaction events when only one actually occurred. The total film thickness separating the detectors must be greater than the sum of $L_{LR} + L_{SR}$ in order to confidently eliminate the possibility of recording coincident particles from a single neutron absorption. The most straightforward method for producing such a device is to simply fasten two front-coated devices together. With identical devices, the neutron sensitive film thickness for each individual detector should range between and $(L_{LR} + L_{SR})/2$ and L_{LR}. If the device is operated in pulse mode, anti-coincidence counting techniques can be used to reduce the probability of recording two counts for one neutron absorption event, thereby lifting the film thickness constraint.

The double-inward facing detector configuration allows for the realization of coincident counts, in which both detectors can detect an ion from the very same neutron absorption. The problem can be remedied with anti-coincident counting electronics if using the devices *individually*, or most easily, by simply connecting the diodes together with one output. If the preamplifier

outputs are connected together, the devices operate as one detector and coincident events produce a single output pulse signal. However, to calculate the expected efficiency, the probability of a coincident event must be subtracted from the summed probabilities that individual reaction product ions will enter the semiconductor detectors. Hence

$$S(D_F)|_{Total} = \sum_{p=1}^{N} S_p(D_F) - \sum_{i=1}^{R} [Q_{iLR,SR}(D_F) + Q_{iSR,LR}(D_F)] \quad (33)$$

where N is the number of different possible reaction products and R is the number of reaction branches (two for ^{10}B and one for ^{6}Li) and Q is the integrated fractional probability that coincident counts occur within film thickness D_F. The subscripts of Q refer to which detector (front or back) that the long-range and short-range particles enter. For instance, $Q_{LR,SR}$ refers to coincidences in which a long-range particle enters the front detector and a coincident count from a short-range particle enters the back detector. Obviously, $Q_{SR,LR}$ refers to the opposite case. Eqs. (18a), (18b), (25a) and (25b) can be used together to determine the values of $S_p(D_F)$, although the integration boundary limits must be administered correctly. Solving for the integrals, the detection probability integrals for a particle entering the *front* detector are

$$\begin{aligned} S_{pF}(D_F) &= \frac{F_p}{4\pi I_0} I_0 \prod_{i=1}^{M} e^{-\Sigma_i D_i} \times \int_0^{2D_F} 2\pi\Sigma_F e^{-x\Sigma_F}\left(1-\frac{x}{L}\right) dx \\ &= 0.5F_p \prod_{i=1}^{M} e^{-\Sigma_i D_i} \times \left\{ \left(1-\frac{1}{\Sigma_F L}\right)(1-e^{-2\Sigma_F D_F}) + \frac{2D_F}{L} e^{-2\Sigma_F D_F} \right\} \\ &\quad \text{for } L \geqslant 2D_F \end{aligned} \quad (34a)$$

and

$$\begin{aligned} S_{pF}(D_F) &= \frac{F_p}{4\pi I_0} I_0 \prod_{i=1}^{M} e^{-\Sigma_i D_i} \int_0^{L} 2\pi\Sigma_F e^{-x\Sigma_F}\left(1-\frac{x}{L}\right) dx \\ &= 0.5F_p \prod_{i=1}^{M} e^{-\Sigma_i D_i} \left\{ \left(1-\frac{1}{\Sigma_F L}\right)(1-e^{-\Sigma_F L}) + e^{-\Sigma_F L} \right\} \\ &\quad \text{for } L \leqslant 2D_F. \end{aligned} \quad (34b)$$

The detection probability integrals for a particle entering the back detector are

$$\begin{aligned} S_{pB}(D_F) &= \frac{F_p}{4\pi I_0} \prod_{i=1}^{M} e^{-\Sigma_i D_i} \int_0^{2D_F} I_0 2\pi\Sigma_F e^{-x\Sigma_F}\left(1-\frac{(2D_F-x)}{L}\right) dx \\ &= 0.5F_p \prod_{i=1}^{M} e^{-\Sigma_i D_i} \left\{ \left(1+\frac{1}{\Sigma_F L}\right)(1-e^{-2\Sigma_F D_F}) - \frac{2D_F}{L} \right\}. \\ &\quad L \geqslant 2D_F \end{aligned} \quad (35a)$$

and

$$\begin{aligned} S_{pB}(D_F) &= \frac{F_p e^{-\Sigma_F(2D_F-L)}}{4\pi I_0} \prod_{i=1}^{M} e^{-\Sigma_i D_i} \times \int_{2D_F-L}^{2D_F} I_0 2\pi\Sigma_F e^{-x\Sigma_F}\left(1-\frac{(2D_F-x)}{L}\right) dx \\ &= 0.5F_p e^{-\Sigma_F(2D_F-L)} \prod_{i=1}^{M} e^{-\Sigma_i D_i} \times \left\{ \left(1+\frac{1}{\Sigma_F L}\right)(1-e^{-\Sigma_F L}) - 1 \right\} \\ &\quad L \leqslant 2D_F. \end{aligned} \quad (35b)$$

For any thickness of D_F, the appropriate equations must be used for each reaction product particle and for each detector, front or back.

After adding the solutions from the appropriate forms of Eqs. (34a), (34b), (35a) and (35b), the reader should understand that coincident events have been included. In other words, many events have been counted twice. The probability of coincident events must be subtracted from the solution shown in Eqs. (34) and (35). Coincident events occur when both particles, after being ejected in opposite directions, are within solid angles that intersect both the front and back detectors. The smallest intersecting solid angle for a single particle determines the coincidence

probability, *not* the addition of solid angles for both particles, and *not* the larger of solid angles intersecting either of the detectors. The appropriate integration range can be found by setting the solid angles for the opposing particles equal. Hence, from Eq. (6), the largest ratio of x/L for L_{LR} or L_{SR} determines the smallest angle. With respect to range along the x-axis (see Fig. 33), the integration limits when the *short-range particle* enters the *front* detector are then defined as:

$$0 \leqslant x \leqslant \frac{2D_F L_{SR}}{L_{LR} + L_{SR}} = \Theta \tag{36a}$$

where the *solid angle of the long-range particle* determines the coincidence probability,

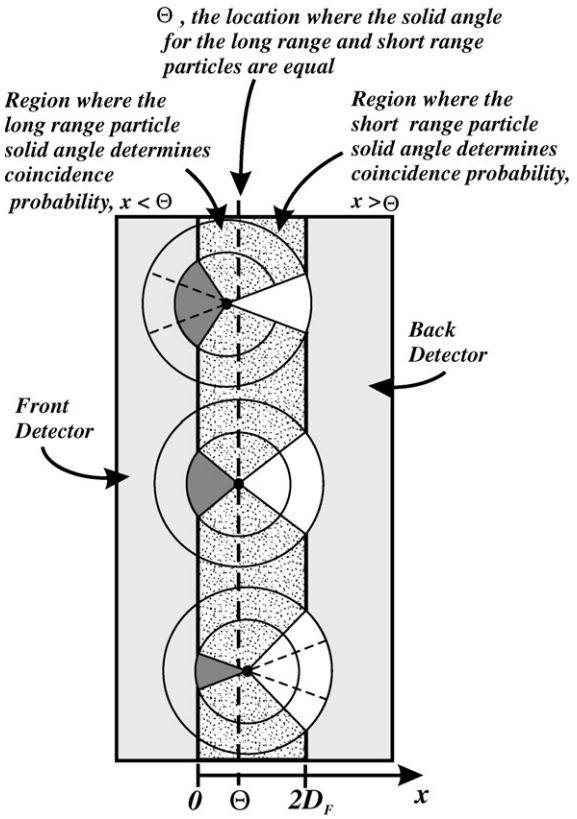

Fig. 33. Diagram depicting coincidence counts when the short-range product enters the front device and the long-range product enters the back device.

and

$$2D_F \geqslant x \geqslant \frac{2D_F L_{SR}}{L_{LR} + L_{SR}} = \Theta \tag{36b}$$

where the *solid angle of the short-range particle* determines the coincidence probability.

The accompanying integrals become particle specific

$$\begin{aligned} Q_{SR,LR}(D_F) &= \frac{F_p}{4\pi I_0} I_0 \prod_{i=1}^{M} e^{-\Sigma_i D_i} \\ &\quad \times \left[\int_0^{\Theta} I_0 2\pi\Sigma_F e^{-x\Sigma_F} \left(1 - \frac{(2D_F - x)}{L_{LR}}\right) dx \right. \\ &\quad \left. + \int_{\Theta}^{2D_F} 2\pi\Sigma_F e^{-x\Sigma_F} \left(1 - \frac{x}{L_{SR}}\right) dx \right] \\ &= 0.5 F_p \prod_{i=1}^{M} e^{-\Sigma_i D_i} \\ &\quad \times \left\{ e^{-\Sigma_F \Theta} \left[\frac{2\Sigma_F D_F - L_{LR}\Sigma_F - \Sigma_F \Theta - 1}{L_{LR}\Sigma_F} \right] \right. \\ &\quad - \left[\frac{2\Sigma_F D_F - L_{LR}\Sigma_F - 1}{L_{LR}\Sigma_F} \right] \\ &\quad + e^{-2\Sigma_F D_F} \left[\frac{2\Sigma_F D_F - L_{SR}\Sigma_F + 1}{L_{SR}\Sigma_F} \right] \\ &\quad \left. + e^{-\Sigma_F \Theta} \left[\frac{L_{SR}\Sigma_F - \Theta\Sigma_F - 1}{L_{SR}\Sigma_F} \right] \right\}, \end{aligned}$$

$$\text{for } 2D_F \leqslant L_{SR} \tag{37a}$$

$$\begin{aligned} Q_{SR,LR}(D_F) &= \frac{F_p}{4\pi I_0} I_0 \prod_{i=1}^{M} e^{-\Sigma_i D_i} \\ &\quad \times \left[\int_0^{\Theta} I_0 2\pi\Sigma_F e^{-x\Sigma_F} \left(1 - \frac{(2D_F - x)}{L_{LR}}\right) dx \right. \\ &\quad \left. + \int_{\Theta}^{L_{SR}} 2\pi\Sigma_F e^{-x\Sigma_F} \left(1 - \frac{x}{L_{SR}}\right) dx \right] \\ &= 0.5 F_p \prod_{i=1}^{M} e^{-\Sigma_i D_i} \\ &\quad \times \left\{ e^{-\Sigma_F \Theta} \left[\frac{2\Sigma_F D_F - \Sigma_F L_{LR} - \Theta\Sigma_{LR} - 1}{\Sigma_F L_{LR}} \right] \right. \\ &\quad - \left[\frac{2\Sigma_F D_F - \Sigma_F L_{LR} - 1}{\Sigma_F L_{LR}} \right] + \left[\frac{e^{-\Sigma_F L_{SR}}}{\Sigma_F L_{SR}} \right] \\ &\quad \left. + e^{-\Sigma_F \Theta} \left[\frac{\Sigma_F L_{SR} - \Sigma_F \Theta - 1}{\Sigma_F L_{SR}} \right] \right\}, \end{aligned}$$

$$\text{for } L_{SR} \leqslant 2D_F \leqslant L_{LR} \tag{37b}$$

$$
\begin{aligned}
Q_{\mathrm{SR,LR}}(D_{\mathrm{F}}) &= \frac{F_{\mathrm{p}}}{4\pi I_0} I_0 \prod_{i=1}^{M} \mathrm{e}^{-\Sigma_i D_i} \\
&\quad \times \left[\int_{2D_{\mathrm{F}}-L_{\mathrm{LR}}}^{\Theta} I_0 2\pi\Sigma_{\mathrm{F}} \mathrm{e}^{-x\Sigma_{\mathrm{F}}} \left(1 - \frac{(2D_{\mathrm{F}} - x)}{L_{\mathrm{LR}}}\right) \mathrm{d}x \right. \\
&\quad \left. + \int_{\Theta}^{L_{\mathrm{SR}}} 2\pi\Sigma_{\mathrm{F}} \mathrm{e}^{-x\Sigma_{\mathrm{F}}} \left(1 - \frac{x}{L_{\mathrm{SR}}}\right) \mathrm{d}x \right] \\
&= 0.5 F_{\mathrm{p}} \prod_{i=1}^{M} \mathrm{e}^{-\Sigma_i D_i} \\
&\quad \times \left\{ \mathrm{e}^{-\Sigma_{\mathrm{F}}\Theta} \left[\frac{2\Sigma_{\mathrm{F}} D_{\mathrm{F}} - \Sigma_{\mathrm{F}} L_{\mathrm{LR}} - \Sigma_{\mathrm{F}}\Theta - 1}{\Sigma_{\mathrm{F}} L_{\mathrm{LR}}} \right] \right. \\
&\quad + \left[\frac{\mathrm{e}^{-\Sigma_{\mathrm{F}}(2D_{\mathrm{F}} - L_{\mathrm{LR}})}}{\Sigma_{\mathrm{F}} L_{\mathrm{LR}}} \right] + \left[\frac{\mathrm{e}^{-\Sigma_{\mathrm{F}} L_{\mathrm{SR}}}}{\Sigma_{\mathrm{F}} L_{\mathrm{SR}}} \right] \\
&\quad \left. + \mathrm{e}^{-\Sigma_{\mathrm{F}}\Theta} \left[\frac{\Sigma_{\mathrm{F}} L_{\mathrm{SR}} - \Sigma_{\mathrm{F}}\Theta - 1}{\Sigma_{\mathrm{F}} L_{\mathrm{SR}}} \right] \right\} \\
&\quad \text{for } L_{\mathrm{LR}} \leqslant 2D_{\mathrm{F}} \leqslant L_{\mathrm{SR}} + L_{\mathrm{LR}} \qquad (37c)
\end{aligned}
$$

$$
Q_{\mathrm{SR,LR}}(D_{\mathrm{F}}) = 0, \quad L_{\mathrm{SR}} + L_{\mathrm{LR}} \leqslant 2D_{\mathrm{F}}. \qquad (37d)
$$

For the *long-range particle* intersecting the *front detector* (see Fig. 34), the integration limits are:

$$
0 \leqslant x \leqslant \frac{2D_{\mathrm{F}} L_{\mathrm{LR}}}{L_{\mathrm{LR}} + L_{\mathrm{SR}}} = \Gamma \qquad (38a)
$$

where the *solid angle of the short-range particle* determines the coincidence probability, and

$$
2D_{\mathrm{F}} \geqslant x \geqslant \frac{2D_{\mathrm{F}} L_{\mathrm{LR}}}{L_{\mathrm{LR}} + L_{\mathrm{SR}}} = \Gamma \qquad (38b)
$$

where the *solid angle of the long-range particle* determines the coincidence probability. The accompanying integrals become particle specific:

$$
\begin{aligned}
Q_{\mathrm{LR,SR}}(D_{\mathrm{F}}) &= \frac{F_{\mathrm{p}}}{4\pi I_0} I_0 \prod_{i=1}^{M} \mathrm{e}^{-\Sigma_i D_i} \\
&\quad \times \left[\int_{0}^{\Gamma} I_0 2\pi\Sigma_{\mathrm{F}} \mathrm{e}^{-x\Sigma_{\mathrm{F}}} \left(1 - \frac{(2D_{\mathrm{F}} - x)}{L_{\mathrm{SR}}}\right) \mathrm{d}x \right. \\
&\quad \left. + \int_{\Gamma}^{2D_{\mathrm{F}}} 2\pi\Sigma_{\mathrm{F}} \mathrm{e}^{-x\Sigma_{\mathrm{F}}} \left(1 - \frac{x}{L_{\mathrm{LR}}}\right) \mathrm{d}x \right] \\
&= 0.5 F_{\mathrm{p}} \prod_{i=1}^{M} \mathrm{e}^{-\Sigma_i D_i}
\end{aligned}
$$

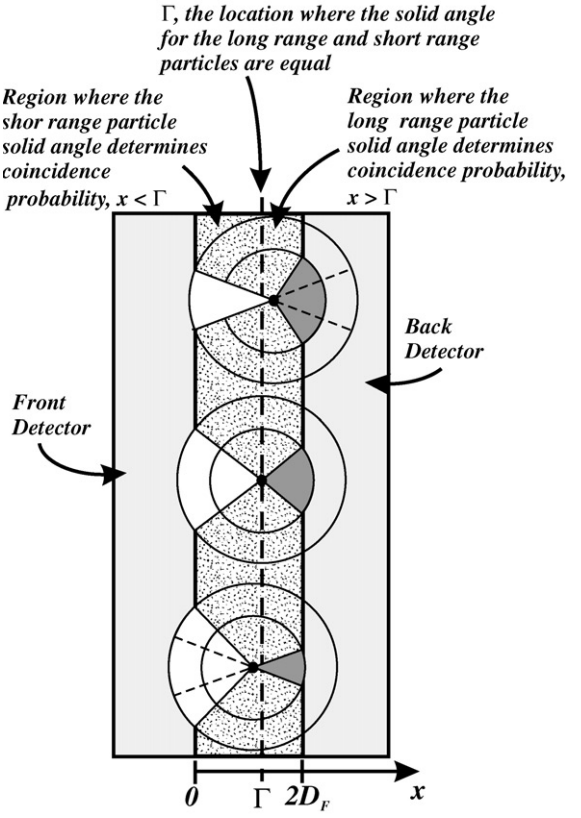

Fig. 34. Diagram depicting coincidence counts when the long-range product enters the front device and the short-range product enters the back device.

$$
\begin{aligned}
&\times \left\{ \mathrm{e}^{-\Sigma_{\mathrm{F}}\Gamma} \left[\frac{2\Sigma_{\mathrm{F}} D_{\mathrm{F}} - \Sigma_{\mathrm{F}} L_{\mathrm{SR}} - \Sigma_{\mathrm{F}}\Gamma - 1}{\Sigma_{\mathrm{F}} L_{\mathrm{SR}}} \right] \right. \\
&\quad - \left[\frac{2\Sigma_{\mathrm{F}} D_{\mathrm{F}} - \Sigma_{\mathrm{F}} L_{\mathrm{SR}} - 1}{\Sigma_{\mathrm{F}} L_{\mathrm{SR}}} \right] \\
&\quad + \mathrm{e}^{-2\Sigma_{\mathrm{F}} D_F} \left[\frac{2\Sigma_{\mathrm{F}} D_{\mathrm{F}} - \Sigma_{\mathrm{F}} L_{\mathrm{LR}} + 1}{\Sigma_{\mathrm{F}} L_{\mathrm{LR}}} \right] \\
&\quad \left. + \mathrm{e}^{-\Sigma_{\mathrm{F}}\Gamma} \left[\frac{\Sigma_{\mathrm{F}} L_{\mathrm{LR}} - \Sigma_{\mathrm{F}}\Gamma - 1}{\Sigma_{\mathrm{F}} L_{\mathrm{LR}}} \right] \right\}, \\
&\text{for } 2D_{\mathrm{F}} \leqslant L_{\mathrm{SR}} \qquad (39a)
\end{aligned}
$$

$$
\begin{aligned}
Q_{\mathrm{LR,SR}}(D_{\mathrm{F}}) &= \frac{F_{\mathrm{p}}}{4\pi I_0} I_0 \prod_{i=1}^{M} \mathrm{e}^{-\Sigma_i D_i} \\
&\quad \times \left[\int_{2D_{\mathrm{F}}-L_{\mathrm{SR}}}^{\Gamma} 2\pi\Sigma_{\mathrm{F}} \mathrm{e}^{-x\Sigma_{\mathrm{F}}} \left(1 - \frac{x}{L_{\mathrm{SR}}}\right) \mathrm{d}x \right.
\end{aligned}
$$

$$+\int_{\Gamma}^{2D_F} I_0 2\pi\Sigma_F e^{-x\Sigma_F}\left(1-\frac{(2D_F-x)}{L_{LR}}\right)dx\Bigg]$$
$$= 0.5F_p\prod_{i=1}^{M} e^{-\Sigma_i D_i}$$
$$\times\left\{e^{-\Sigma_F\Gamma}\left[\frac{2\Sigma_F D_F-\Sigma_F L_{SR}-\Sigma_F\Gamma-1}{\Sigma_F L_{SR}}\right]\right.$$
$$+\left[\frac{e^{-(2D_F-L_{SR})\Sigma_F}}{\Sigma_F L_{SR}}\right]$$
$$+e^{-2\Sigma_F D_F}\left[\frac{2\Sigma_F D_F-\Sigma_F L_{LR}+1}{\Sigma_F L_{LR}}\right]$$
$$\left.+e^{-\Sigma_F\Gamma}\left[\frac{\Sigma_F L_{LR}-\Sigma_F\Gamma-1}{\Sigma_F L_{LR}}\right]\right\}$$
$$\text{for } L_{SR}\leqslant 2D_F\leqslant L_{LR} \tag{39b}$$

$$Q_{LR,SR}(D_F) = \frac{F_p}{4\pi I_0} I_0\prod_{i=1}^{M} e^{-\Sigma_i D_i}$$
$$\times\left[\int_{2D_F-L_{SR}}^{\Gamma} 2\pi\Sigma_F e^{-x\Sigma_F}\left(1-\frac{x}{L_{LR}}\right)dx\right.$$
$$\left.+\int_{\Gamma}^{L_{LR}} I_0 2\pi\Sigma_F e^{-x\Sigma_F}\left(1-\frac{(2D_F-x)}{L_{SR}}\right)dx\right]$$
$$= 0.5F_p\prod_{i=1}^{M} e^{-\Sigma_i D_i}$$
$$\times\left\{e^{-\Sigma_F\Gamma}\left[\frac{2\Sigma_F D_F-\Sigma_F L_{SR}-\Sigma_F\Gamma-1}{\Sigma_F L_{SR}}\right]\right.$$
$$+\left[\frac{e^{-(2D_F-L_{SR})\Sigma_F}}{\Sigma_F L_{SR}}\right]+\left[\frac{e^{-\Sigma_F L_{LR}}}{\Sigma_F L_{LR}}\right]$$
$$\left.+e^{-\Sigma_F\Gamma}\left[\frac{\Sigma_F L_{LR}-\Sigma_F\Gamma-1}{\Sigma_F L_{LR}}\right]\right\}$$
$$\text{for } L_{LR}\leqslant 2D_F\leqslant L_{SR}+L_{LR} \tag{39c}$$

$$Q_{LR,SR}(D_F)=0,\quad L_{SR}+L_{LR}\leqslant 2D_F. \tag{39d}$$

The possibility of coincident counts is eliminated for the condition $(L_{SR}+L_{LR})\leqslant 2D_F$. The appropriate combinations of Eqs. (34)-(39) can describe the neutron detection efficiency of the device. Figs. 35–37 show comparison efficiencies for sandwich devices, both double-outward and double-inward facing designs, coated with ^{10}B, ^{6}LiF, and pure ^{6}Li films. Both methods of producing higher efficiency are valid. Note that neutron absorption in the contacts and the detector bulk should be accounted for when designing the device, especially in cases where the contact and/or detector materials have relatively large neutron attenuation cross-sections. The reader is directed to inspect the obvious improvement for the double-inward facing device structure over the double-outward facing (front and back coated) device structure. Not only is there a slight increase in efficiency for the double-inward facing device design, but also the film thickness per each device required for optimum performance is less. For instance, in Fig. 35, given the 300 keV LLD requirement, outward-facing

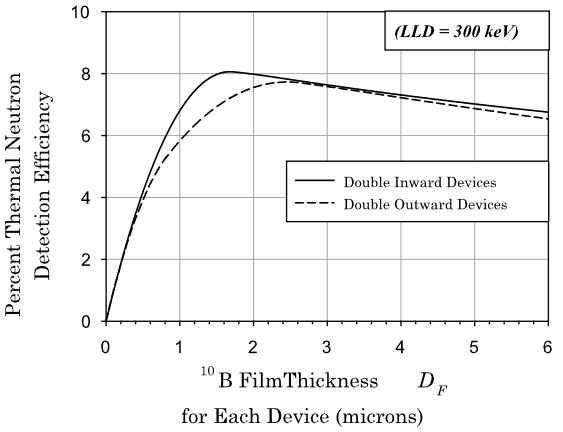

Fig. 35. Comparison thermal neutron detection efficiencies for ^{10}B-coated devices using the double-inward and the double-outward designs.

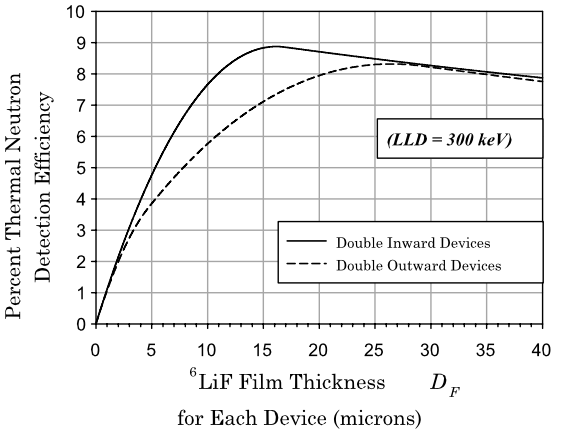

Fig. 36. Comparison thermal neutron detection efficiencies for ^{6}LiF–coated devices using the double-inward and the double-outward designs.

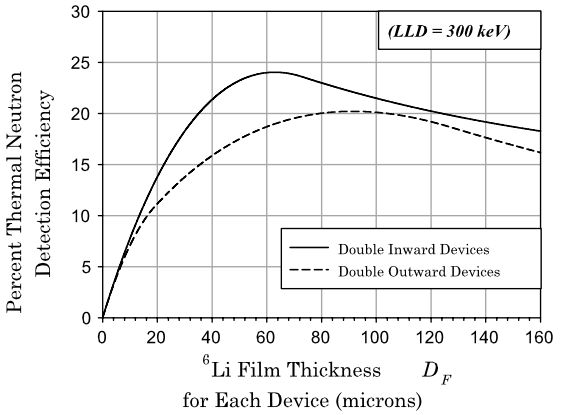

Fig. 37. Comparison thermal neutron detection efficiencies for ^{6}Li-coated devices using the double-inward and the double-outward designs.

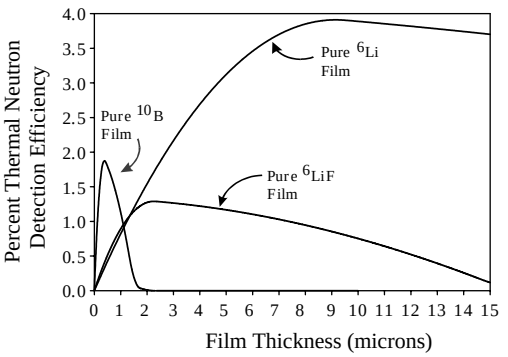

Fig. 38. The expected thermal neutron detection efficiency as a function of film thickness for double-inward devices operated in coincidence.

^{10}B-coated devices need to have a film thickness of 2.4 μm *each* to achieve a maximum thermal neutron efficiency of 7.73%, whereas inward-facing devices need to have a film thickness of only 1.7 μm each to achieve a maximum thermal neutron detection efficiency of 8.06%. Figs. 36 and 37 show similar improvements for ^{6}LiF films and pure ^{6}Li films. Hence, the double-inward sandwich design is best for thermal neutron detection optimization.

Attempts to utilize the coincidence feature for double-inward facing devices have been reported [34]. Background radiation interference can be significantly decreased by including only those counts that enter the opposing devices in coincidence, which can be performed in a straightforward fashion with a commercial coincidence analyzer. The expected efficiency from such a system can be calculated from Eqs. (36)-(39), in which *only* the coincident counts contribute to neutron detection.

Fig. 38 shows the calculated thermal neutron detection efficiency for double-inward facing devices operated in coincidence mode as a function of film thickness on *each* detector. Hence, the total converter thickness between the two inward-facing detectors would be twice that shown on the graph *x*-axis. The reader is directed to notice that pure ^{10}B-based films can achieve higher neutron detection efficiencies than ^{6}LiF-based films, with pure ^{6}Li-based films yielding the highest overall neutron detection efficiencies. It should also be noticed that the maximum thermal neutron detection efficiency achievable is dramatically lower than previous cases, being only 1.87% for ^{10}B films, 1.29% for ^{6}LiF films, and 3.91% for ^{6}Li films.

To summarize, the double-coated device structures will yield efficiency improvements for thermal neutron detection. The double-coated (front and back) and the double-outward facing devices have no issues with coincident neutron detection events; yet they have lower maximum achievable thermal neutron efficiencies. Also, double-coated outward facing devices require higher operating voltages since the device active region (or depletion region) must extend across the entire detector. The double-inward facing device structure requires lower operating voltages than double-sided devices, and the structure allows for higher thermal neutron detection efficiencies, all with thinner reactive film requirements than needed for the double-outward facing designs.

An advanced form of the double-inward facing design uses double-coated detectors. For instance, two devices with ^{6}LiF/^{10}B films are faced into each other and operated as a single device. Employing the concepts described in the previous sections, it can be shown that a ^{6}LiF/^{10}B system can achieve a thermal neutron detection efficiency exceeding 13.5%, and a ^{6}Li/^{10}B system can achieve a thermal neutron detection efficiency exceeding 25%, both with the standard LLD setting of 300 keV.

Additional assemblies can be made that also use stacks of the devices to further increase the detection efficiency, hence is entirely reasonable to expect 25% thermal neutron detection efficiencies from compact, thin-film-coated, semiconductor detectors with device configurations less than one mm in total thickness.

6. Experimental verification

6.1. Detector fabrication

Schottky barrier bulk GaAs diodes were manufactured for experimental comparisons of theoretical values. A variety of other semiconductor substrates can be used, such as SiC, Si, or diamond, yet bulk GaAs devices are very easy to manufacture and are actually less costly than devices fabricated from zone-refined Si. The GaAs diodes were manufactured in the following manner. Bulk semi-insulating (SI) GaAs wafers were acquired from American Xtal Technologies (AXT). The back surfaces were lapped at 30 rpm with 3 μm calcined aluminum oxide powder/de-ionized water solution over an optically flat glass plate until 100 μm of GaAs material was removed. Afterwards, the backsides were polished with 0.3 μm calcined aluminum oxide powder mixed in a sodium hypochlorite solution (trade name "Chemlox" [35]) over a chemically resistant polishing cloth ("Chemcloth"[35]) at 65 rpm for 10 min. A final polish was performed with a methyl alcohol (250 ml): glycerol (250 ml): bromine (5 ml) solution for 10 min over another Chemcloth polishing pad at 70 rpm. The wafers were cleaned in a series of solvents and etched in a H_2SO_4 (1 ml): H_2O_2 (1 ml): de-ionized water (320 ml) solution for 5 min followed by a 2 min etch in a HCl (200 ml): de-ionized water (200 ml) solution. The wafers were then cleaned in a de-ionized water cascade and blown dry with N_2.

Two methods were used to produce low resistivity n-type contacts on the backsides of the devices. In the more traditional manner, a layered combination of Ni, Au, and Ge was evaporated onto the polished and etched GaAs surfaces. The evaporated contacts were subsequently sintered for 1 min at 400°C in argon to produce a low-resistivity ("ohmic") contact [36].

With a lower temperature procedure, the backsides were implanted at an angle of 7° from normal with ^{29}Si ions at energies of 50, 100, and 180 keV with doses amounting to 4×10^{13} ions per cm^2, 5×10^{13} ions per cm^2 and 6×10^{13} ions per cm^2, respectively. The implants were activated with a rapid thermal anneal in Ar for 30 s at 800°C. Afterwards, a stacked layer of Ge (500 Å): Pd (1300 Å) was vacuum evaporated over the backsides, followed by a low temperature anneal of 250°C in N_2 for 30 min. Vacuum evaporation of a stacked layer of Ti (150 Å): Au (700 Å) completed backside processing of the devices.

Front side processing of the devices included lapping and polishing of the samples. The initial lapping with 3 μm calcined aluminum oxide powder was used to thin the wafers to 250 μm total thickness. Next, the wafers were polished using the 0.3 μm calcined aluminum oxide powder mixed in a sodium hypochlorite solution followed by the methyl alcohol (250 ml): glycerol (250 ml): bromine (5 ml) solution as previously described. Again, the wafers were cleaned in a series of solvents and etched in a H_2SO_4 (1 ml): H_2O_2 (1 ml): de-ionized water (320 ml) solution for 5 min followed by a 2 min etch in a HCl (200 ml): de-ionized water (200 ml) solution. Care was taken to coat the backsides with photoresist to prevent the acid solution from attacking the previously processed surfaces. Afterwards, the wafers were cleaned in a de-ionized water cascade and blown dry with N_2.

Circular defined patterns of 3.5 mm diameter were patterned onto the surface with photoresist. Photoresist residue in the patterns was removed in oxygen plasma for 2 min. A final etch in the circular patterns was performed with the H_2SO_4 (1 ml): H_2O_2 (1 ml): de-ionized water (320 ml) solution (5 min again) followed by the HCl (200 ml): de-ionized water (200 ml) solution (2 min). The wafers were washed in a de-ionized water cascade and blown dry with N_2. A stacked layer of Ti (150 Å): Au (450 Å) was evaporated over the wafer and lifted off in acetone. Circular photoresist defined patterns of 3 mm diameter were centered and patterned over the Ti/Au metal

Schottky contacts. Undeveloped residue in the photoresist patterns was removed in an oxygen plasma for 2 min. The wafers were fastened to a chilled plate in a vacuum evaporator and 98% isotopic enriched ^{10}B was vacuum evaporated over the Schottky contacts. Each wafer sample received a different ^{10}B deposition thickness, ranging from 1000 Å up to 2 μm. After evaporation, the residue was lifted off in acetone, leaving behind a layer of ^{10}B fastened to the front Schottky contact.

The ^{10}B film applied onto the diode blocking contacts by an electron beam evaporator ensures accuracy in the film thickness. Furthermore, precise features for small, single pad detectors and pixel detectors are easily achieved with a lift-off process when using evaporation techniques [37]. Achieving the correct ^{10}B film thickness is critical for optimum performance, and undershooting or overshooting the proper thickness will result in decreased neutron detection efficiency, as shown in previous sections. Unfortunately, achieving the optimum ^{10}B thickness of 2.4 μm through evaporation methods has been elusive until recently. For flat surface devices, the ^{10}B film becomes stressed in evaporated layers greater than approximately 1 μm, which causes cracking and peeling [38]. Consequently, ^{10}B coatings were generally held at 1 μm or less, thereby limiting the thermal neutron detection efficiency to only 2.9%. However, a new method of surface preparation that utilizes tiny etched holes has allowed for the deposition of films up to 4 μm thick with repeatable and very reliable results [38], and was used successfully for some devices described later. Fig. 39 shows the general diode configuration for a SI bulk GaAs neutron detector.

The individual devices were cleaved from the GaAs wafers, and fastened with Ag-based epoxy to 1 mm thick aluminum oxide mounts. The mounts were designed with a 3.8 mm hole in the center, around which a Ti (300 Å)/ Au (3000 Å) contact had been evaporated. The devices were mounted with the backside attached to the alumina substrate holder, and the front side facing out. The hole in the center of the alumina mount was designed to reduce neutron absorption or scattering effects that might alter the measurement accuracy. The detectors were then mounted into aluminum light impenetrable boxes to perform the neutron measurements.

Double-coated detectors were fabricated from both ^{6}LiF and ^{6}Li laid upon ^{10}B films. The devices

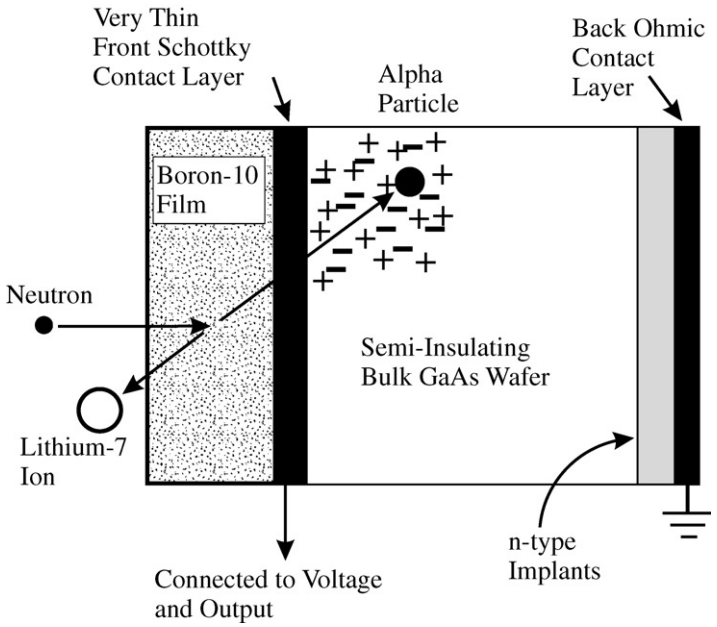

Fig. 39. The basic structure of a SI GaAs Schottky barrier device.

were fabricated as described previously, but with approximately 1 μm of ^{10}B upon the detector. Afterwards, polished samples of ^{6}LiF were attached to the front of the devices with epoxy. An overcoat of Humiseal was applied to prevent possible delamination.

Devices fabricated with pure ^{6}Li required special handling [33]. Pure ^{6}Li, kept in mineral oil, was placed along with a hot plate, a custom stainless steel press, and hollow brass punch, wax paper, and xylene in a plastic glove box. Argon was plumbed into the glove box and allowed to flow for 15 min. A piece of ^{6}Li was removed from its container and a small slice removed with a razor blade, followed by cleaning (to remove the mineral oil) in xylene. The slice was placed between two small squares of wax paper and then into the stainless steel press with calibrated parts to press films ranging from 50 to 100 μm thick. After pressing, small circles 3 mm in diameter were punched from the flattened material and placed upon the ^{10}B films of the prepared detectors. The devices were then transferred to a hot plate and more wax paper was placed over them. A small weight was placed over the samples to keep the ^{6}Li circles flat. The hot plate was warmed to 180°C so that the ^{6}Li attached itself to the ^{10}B film. Afterwards, a piece of Kapton tape was applied to the detector to cover the ^{6}Li disc, followed by Humiseal. Unfortunately, even with the sealing precautions, the ^{6}Li still decomposed within two weeks, yet measurements were made that provided meaningful detection efficiency data.

Sandwich and compound devices were fabricated as indicated above with the following differences. Output Au wires were first attached to all devices. Simple sandwich designs were fabricated by placing a bare detector, facing inward, atop a coated detector and then fastening the two together with insulating epoxy. The output wires were attached together, anode to anode and cathode to cathode. Compound designs were fabricated by placing thin polished samples (20–30 μm) of ^{6}LiF between two inward-facing ^{10}B-coated devices. The samples were fastened together with insulating epoxy and the output wires attached as previously described.

6.2. Characterization

Detector characterization was conducted at the University of Michigan Ford Nuclear Reactor, with beam port 'A'. As shown in Fig. 40, neutrons from the nuclear reactor are thermalized in a D_2O tank. Beam port 'A' points into the D_2O tank, but in such a fashion that it does not point at the reactor. As a result, the gamma ray background component is significantly decreased below that of the other available beam ports. The neutron beam is then diffracted twice to further remove it from background gamma rays. Although the thermal neutron beam emerging from the double diffractometer in beam port 'A' has a low gamma ray background component, it also has a low neutron flux.

Before any measurements began, a fission chamber was used to measure the neutron flux emerging from the A-port which gave a value of

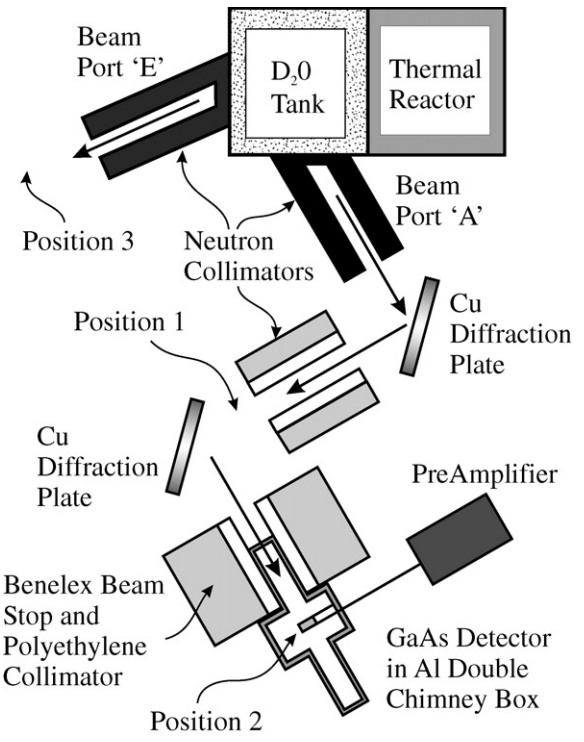

Fig. 40. The experimental configuration for testing the thermal neutron detectors. The aluminum chimney box ensured consistent alignment within the neutron beam.

approximately $\Phi = 2.7 \times 10^4$ n/cm^2 s. Due to control rod movements over the period in which the GaAs neutron detectors were tested, it is expected that the neutron flux value also changed with time. Adjacent beam port experiments also contributed to changes in neutron background. The changes in the neutron flux may amount to a few percent (2–3%), hence the neutron flux value quoted represents only an average measurement.

The mounted devices were installed into aluminum testing boxes designed to reduce radiofrequency (RF) and photoelectric noise [27,39]. The boxes have two cylindrical, close-ended, hollow chimneys opposite each other on the front and on the back. The chimney box design enables repeatable indexing of the detectors by ensuring a standardized and fixed location in the thermal neutron beam. Each detector was mounted in order that the Schottky contact was centered relative to the hollow chimneys and furthermore that the detector plane was centered within the chimney box. The closed, light impenetrable box was inserted into a HDPE collar that fit snugly into the receiving end of the neutron beam port collimator block. The detector was connected through the aluminum box to an Ortec 142A preamplifier. The signals were shaped in an amplifier and recorded on a multichannel analyzer. One-hour duration measurements were performed, and the dead time was adjusted and maintained at 2%.

Detectors with various ^{10}B film thicknesses were tested for both reaction product spectral changes and neutron counting efficiency. Both sides of the detector were tested facing the neutron beam: the Schottky contact side was first tested followed by the ohmic contact side. Although the ohmic contact side did not have a ^{10}B coating on it, thermal neutrons pass through the GaAs detector and still become absorbed in the ^{10}B film [25,40], thus allowing for the reaction product emissions to be detected. The electronics remained unchanged throughout the testing, and all measurements were conducted for a "live time" of 1 h. For the Schottky contact side irradiation (front side), Fig. 41 shows pulse height spectra from ^{10}B(n,α)^{7}Li reactions for ^{10}B films ranging from 0.1750 μm to 1.84 μm. The various spectra show the energy peaks for the alpha particle and lithium ion emissions. It is also apparent that total counts under the curves increase with increasing ^{10}B thickness. Also, the reaction products' energy

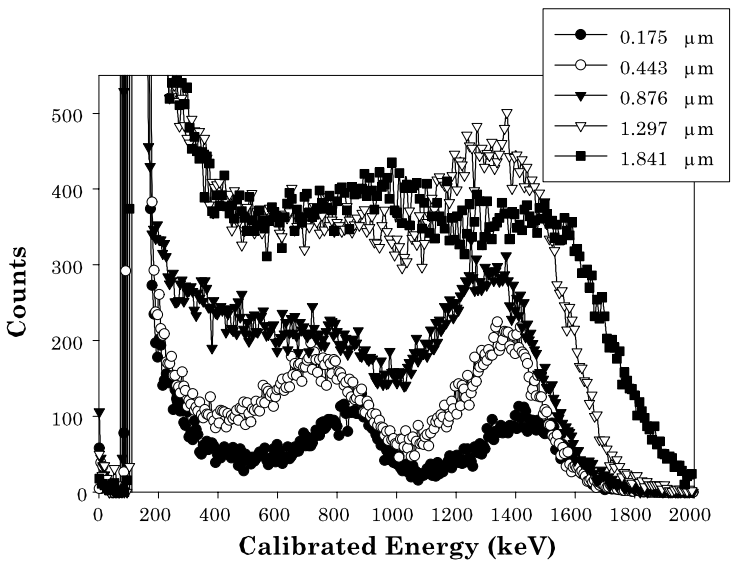

Fig. 41. Spectra taken with ^{10}B-coated SI bulk GaAs detectors of neutron reactions. The data shows the detector response for frontal exposure to a doubly diffracted thermal neutron beam ($\Phi = 2.7 \times 10^4$ n/cm^2 s). The spectral changes as a function of ^{10}B thickness are apparent. Energy peak resolution is best for thin ^{10}B films, whereas efficiency is highest for the thickest ^{10}B films.

peaks become less distinct with increasing ^{10}B thickness, the expected result of reaction-product energy self-absorption within the ^{10}B film. To illustrate, two distinct energy peaks (840 keV ^{7}Li ion and 1.47 MeV α-particle) are present for the 0.1750 μm coated device, yet neither energy peak is discernable for the 1.84 μm-coated device. By summing the number of counts in the channels exceeding 300 keV, the efficiency was determined for several devices as a function of ^{10}B-film thickness for both obverse and reverse irradiations (see Fig. 42). Also shown is the theoretical thermal neutron efficiency curve for an LLD setting of 300 keV, the efficiency curve having been calculated from Eqs. (18) and (19). Fig. 42 shows good agreement with the developed theory and the measurements.

Fig. 43 shows comparison thermal neutron reaction spectra from two detectors, one coated with ^{10}B and the other coated with ^{6}LiF. Both devices were backside irradiated, allowing for maximum neutron detection efficiency. The ^{10}B-coated device (*not* optimized at 1.1 μm of ^{10}B) had a measured thermal neutron detection efficiency of 3.0%, whereas the ^{6}LiF-coated device (35 μm of ^{6}LiF) had a measured thermal neutron detection efficiency of 4.6%. Although the efficiencies are similar, it is important to note that the energy distribution for the ^{6}LiF-coated device is much higher than the ^{10}B-coated device. If the detectors

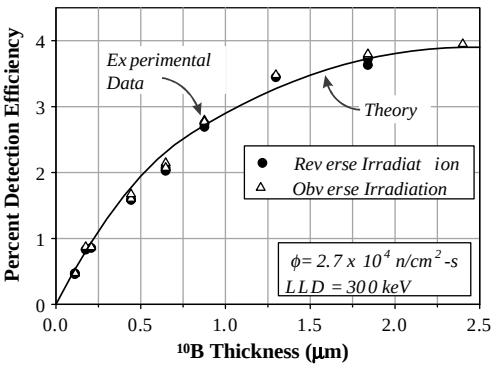

Fig. 42. Thermal neutron detection efficiency for ^{10}B-coated SI bulk GaAs detectors as a function of ^{10}B thickness. The ^{10}B-coated GaAs detectors were irradiated with a doubly diffracted thermal neutron beam ($\Phi = 2.7 \times 10^4$ n/cm^2 s). The LLD was set at 300 keV equivalent.

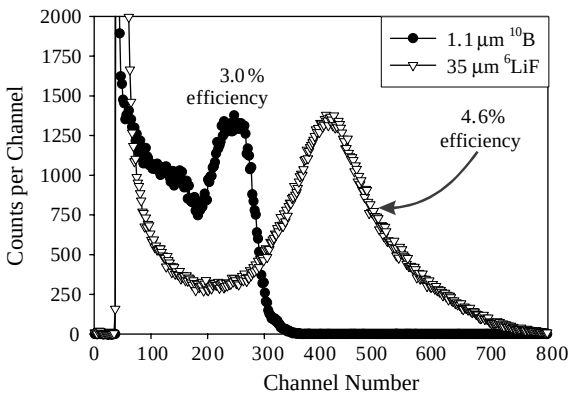

Fig. 43. Comparison neutron reaction product spectra from ^{10}B-coated and ^{6}LiF-coated detectors. The ^{10}B-coated device has only 1.1 μm of material whereas the ^{6}LiF-coated device has 35 μm of material. Gamma-ray discrimination with the LLD is more effective for the ^{6}LiF-coated detector.

are operated in a mixed neutron and gamma ray field, the ^{6}LiF-coated device can operate with the LLD set higher than the ^{10}B-coated device while losing only a small portion of the spectrum (and detection efficiency). Hence, ^{6}LiF-coated devices can provide better gamma ray discrimination than ^{10}B-coated devices.

The double-inward-facing design yields the highest efficiency for sandwich detectors. It does not rely on the full depletion of the detectors and can still be operated with modest operating voltages. Erroneous coincident recordings are avoided by simply connecting the output of both devices to a common input preamplifier. Fig. 44 shows comparison neutron reaction spectra between a single-coated device and a double-inward-facing device, both having ^{6}LiF as the film. With a 35-μm thick ^{6}LiF film, the single device yielded 4.6% thermal neutron detection efficiency. With only 30 μm of ^{6}LiF material between two devices, the double-inward facing configuration yielded 8.95% thermal neutron detection efficiency.

Tests were also performed with the double-layered film configuration, with either ^{6}LiF on 1.1 μm of ^{10}B or pure ^{6}Li on 1.1 μm of ^{10}B. The charged-particle reaction products emanating from ^{10}B(n,α)^{7}Li reactions can reach the detector as with a single-coated device since the film is applied directly to the detector contact. The longer

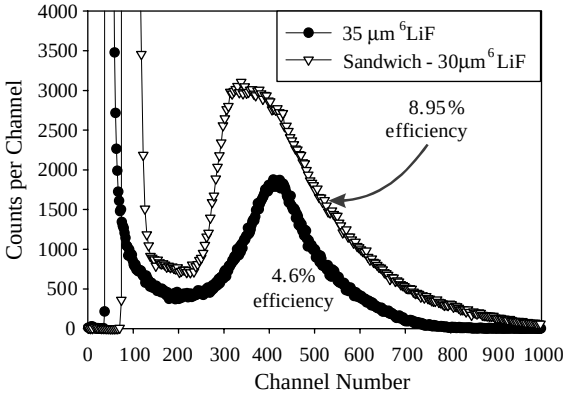

Fig. 44. Shown is a comparison of neutron reaction product spectra from a single-coated device (count time corrected) and a double-inward facing sandwich device. ^{6}LiF layers are used as the converters.

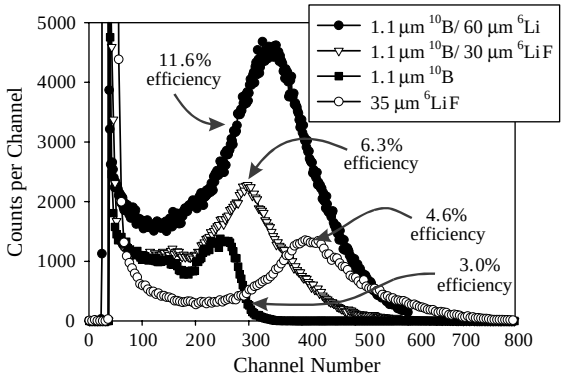

Fig. 45. Comparison neutron reaction product spectra from a ^{10}B single-coated device, a ^{6}LiF single-coated device, and two double-coated devices using ^{10}B/^{6}LiF and ^{10}B/^{6}Li systems.

range charged-particle products emanating from ^{6}Li(n,α)^{3}H reactions can still reach detector even though they must transit through the ^{10}B film as well. However, energy loss occurs, thereby shifting the energy spectrum of the ^{6}Li(n,α)^{3}H reaction products. Fig. 45 shows comparisons between devices with single coatings of ^{10}B and ^{6}LiF, and double coatings of ^{10}B/^{6}LiF and ^{10}B/^{6}Li.

The compound design takes advantage of all of the aforementioned techniques, in which two devices with double-coatings are assembled together in the double-inward facing detector design. To assist with thin-film adhesion, the tiny-hole

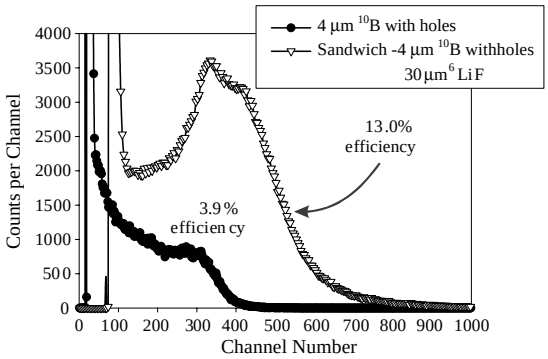

Fig. 46. Comparison neutron reaction product spectra from a via hole covered (10.6%) ^{10}B single-coated device and a compound device that uses both ^{10}B-filled via holes (10.6% coverage) and a ^{6}LiF film combined in a double-coated and double-inward sandwich design.

surface preparation technique was employed for the devices [38], in which 10% of the surface was covered with 3-mm diameter, ^{10}B-filled holes [38]. All detectors had 4-μm thick ^{10}B layers, and the double-coated, double-inward facing device had a 30-μm thick film of ^{6}LiF in the center. The device with only a single coating of ^{10}B was backside irradiated to give optimum performance. Fig. 46 shows comparison neutron reaction product spectra between a single-coated device with that of a ^{10}B/^{6}LiF double layer, double-inward-facing detector. Although the compound device parameters are *not* optimized, the efficiency has more than *tripled* over that of the common ^{10}B-coated device.

7. Conclusions

The basic configurations and expected efficiencies for planar style thin-film-coated semiconductor neutron detectors have been described. A variety of simple methods are available to increase the thermal neutron detection efficiency of thin-film-coated semiconductor neutron detectors. Individually the methods offer respectable efficiency increases. For instance, the basic configurations allow for optimized thermal neutron detection efficiencies ranging from 4% up to 11.6%, depending upon the thin-film selected as the

neutron converter. If the detection efficiency enhancing techniques are used together, dramatic increases in thermal neutron detection efficiency can be realized. For instance, a compound device using a $^{6}LiF/^{10}B$ system can achieve a thermal neutron detection efficiency exceeding 13.5%, whereas a compound device using a $^{6}Li/^{10}B$ can achieve thermal neutron detection efficiencies exceeding 25%. Neutron imaging arrays using the improved technology are also under investigation. The devices are relatively inexpensive to produce, mechanically rugged, and are reliable. Additionally, thermal neutron detection arrays can be developed and fabricated onto single semiconductor wafers as a result of the technological maturity, thereby allowing for the production of compact pixilated imaging systems [2,9,10,20–23,41].

Acknowledgements

The presented work was partially funded by the following grants: DOE Nuclear Engineering Education and Research Grant DE-FG07-98ID13633 and Argonne National Laboratory Subcontracts (DOE) 991262402 and 2F-01141. This research was partially performed under appointment to the US Department of Energy Nuclear Engineering and Health Physics Fellowship Program sponsored by DOE's Office of Nuclear Energy, Science, and Technology.

The neutron detectors were fabricated at the Semiconductor Materials and Radiological Technologies (S.M.A.R.T.) Laboratory (now at Kansas State University) and the Solid State Electronics Laboratory (SSEL) at the University of Michigan.

References

[1] W. Price, Nuclear Radiation Detection, 2nd Edition, McGraw-Hill, New York, 1964.
[2] P. Convert, J.B. Forsyth, Position-Sensitive Detection of Thermal Neutrons, Academic Press, New York, 1983.
[3] N. Tsoulfanidis, Measurement and Detection of Radiation, 2nd Edition, Taylor and Francis, New York, 1995.
[4] G.F. Knoll, Radiation Detection and Measurement, 3rd Edition, Wiley, New York, 2000.
[5] D.I. Garber, R.R. Kinsey, BNL 325: Neutron Cross Sections, 3rd Edition, Vol. 2, Curves, Brookhaven National Laboratory, Upton, 1976.
[6] V. McLane, C.L. Dunford, P.F. Rose, in: Neutron Cross Sections, Vol. 2, Academic Press, San Diego, 1988.
[7] B. Feigl, H. Rauch, Nucl. Instr. and Meth. 61 (1968) 349.
[8] T. Aoyama, Y. Oka, K. Honda, C. Mori, Nucl. Instr. and Meth. A 314 (1992) 590.
[9] A. Mireshghi, G. Cho, J. Drewery, T. Jing, S.N. Kaplan, V. Perez-Mendez, D. Wildermuth, IEEE Trans. Nucl. Sci. NS-39 (1992) 635.
[10] A. Mireshghi, G. Cho, J.S. Drewery, W.S. Hong, T. Jing, H. Lee, S.N. Kaplan, V. Perez-Mendez, IEEE Trans. Nucl. Sci. NS-41 (1994) 915.
[11] F. Foulon, P. Bergonzo, A. Brambilla, C. Jany, B. Guizard, R.D. Marshall, Proc. MRS 487 (1998) 591.
[12] A.G. Vradii, M.I. Krapivin, L.V. Maslova, O.A. Matveev, A.Kh. Khusainov, V.K. Shashurin, Sov. Atomic Energy 42 (1977) 633.
[13] D.S. McGregor, J.T. Lindsay, R.W. Olsen, Nucl. Instr. and Meth. A 381 (1996) 498.
[14] M.A. Lone, R.A. Levitt, D.A. Harrison, Atomic Data Nucl. Data Tables 26 (1981) 511.
[15] J.K. Tuli, Thermal-Neutron-Capture Gamma Rays, BNL-NCS-51647 Report, UC-34-C, Brookhaven National Laboratory, Upton, 1983.
[16] A.J. Peurrung, Nucl. Instr. and Meth. A 443 (2000) 400.
[17] A. Rose, Nucl. Instr. and Meth. 52 (1967) 166.
[18] I.C. Rickard, Nucl. Instr. and Meth. 113 (1973) 169.
[19] R.L. Schulte, F. Swanson, M. Kesselman, Nucl. Instr. and Meth. A 353 (1994) 123.
[20] D.S. McGregor, J.T. Lindsay, C.C. Brannon, R.W. Olsen, IEEE Trans. Nucl. Sci. NS-43 (1996) 1357.
[21] J. Schelten, R. Reinartz, R. Engels, M. Balzhäuser, J. Lauter, W. Schäfer, K.D. Müller, Nucl. Instr. and Meth. A 389 (1997) 447.
[22] S. Pospisil, B. Sopko, E. Harrankova, Z. Janout, J. Konicek, I. Macha, J. Pavlu, Radiat. Prot. Dosim. 46 (1993) 115.
[23] M. Campbell, E.H.M. Heijne, J. Kubasta, P. Middelkamp, S. Pospísil, P. Sícho, W. Snoeys, V. Vrba, Nucl. Instr. and Meth. A 395 (1997) 457.
[24] C. Petrillo, F. Sacchetti, O. Toket, N.J. Rhodes, Nucl. Instr. and Meth. A 378 (1996) 541.
[25] D.S. McGregor, R.T. Klann, H.K. Gersch, Y.-H. Yang, Nucl. Instr. and Meth. A 466 (2001) 126.
[26] R.T. Klann, D.S. McGregor, Conference Record of ICONE-8, No. 8110, 8th International Conference on Nuclear Engineering, April 2-6, 2000, Baltimore, MD, USA.
[27] D.S. McGregor, S.M. Vernon, H.K. Gersch, S.M. Markham, S.J. Wojtczuk, D.K. Wehe, IEEE Trans. Nucl. Sci. NS-47 (2000) 1364.
[28] D.S. McGregor, R.T. Klann, H.K. Gersch, J.D. Sanders, Conference Record of the IEEE Nuclear Science Symposium, Nov. 4–9, 2001, San Diego, CA, USA.

[29] R.D. Evans, The Atomic Nucleus, McGraw-Hill, New York, 1955.
[30] I. Kaplan, Nuclear Physics, 2nd Edition, Addison-Wesley, Reading, 1962.
[31] J.R. Lamarsh, Introduction to Nuclear Reactor Theory, Addison-Wesley, Reading, 1972.
[32] J.F. Ziegler, J.P. Biersack, SRIM-2000 Code, Version 9, IBM Company, 1998.
[33] C.R. Hammond, in: R.C. Weast (Ed.), Handbook of Chemistry and Physics, 58th Edition, CRC Press, West Palm Beach, 1978.
[34] A. Ndoye, F. Cosset, B. Barelaud, C. Celerier, J.L. Decossas, J.C. Vareille, Nucl. Instr. and Meth. A 423 (1999) 414.
[35] Consumable Materials Catalogue, Logitech Product Group, 810 Sharon Drive, Westlake, Ohio, USA, 1996.
[36] D.S. McGregor, G.F. Knoll, Y. Eisen, R. Brake, in: C. del Papa, P.G. Pelfer, K. Smith (Eds.), GaAs Detectors and Electronics for High Energy Physics, Singapore, World Scientific, 1992, p. 30.
[37] R.C. Jaeger, Introduction to Microelectronic Fabrication, Reading, Addison-Wesley, 1993.
[38] D.S. McGregor, R.T. Klann, H.K. Gersch, E. Ariesanti, J.D. Sanders, B. VanDerElzen, IEEE Trans. Nuclear Science 49 (2002) 1999.
[39] H.K. Gersch, D.S. McGregor, P.A. Simpson, Nucl. Instr. and Meth. A 489 (2002) 85.
[40] D.S. McGregor, H.K. Gersch, J.D. Sanders, R.T. Klann, J.T. Lindsay, J. Korean Assoc. Radiat. Prot. 26 (2001) 167.
[41] J.D. Sanders, J.T. Lindsay, D.S. McGregor, Conference Record of the IEEE Nuclear Science Symposium, San Diego, California, Nov. 4–9, 2001.